Multi-Material Fiber Fabrication and Applications in Distributed Sensing

Li Yu

Dissertation submitted to the faculty of the Virginia Polytechnic Institute and State University in partial fulfillment of the requirements for the degree of

Doctor of Philosophy
In
Electrical Engineering

Anbo Wang, Chair
Xiaoting Jia
Yizhen Zhu
Luke F. Lester
Gary R. Pickell

December 11, 2018
Blacksburg

Keywords: Polymer fiber, pressure sensor, temperature sensor

Multi-Material Fiber Fabrication and Applications in Distributed Sensing

Li Yu

ABSTRACT

Distributed sensing has been an attractive alternative to the traditional single-point sensing technology when measurement at multiple locations is required. Traditional distributed sensing methods based on silica optical fiber and electric coaxial cables have some limitations for specific applications, such as in smart textiles and wearable sensors. By adopting the fiber thermal drawing technique, we have designed and fabricated multi-material electrode-embedded polymer fibers with distributed sensing capabilities. Polymers sensitive to temperature and pressure have been incorporated into the fiber structure, and thin metal electrodes placed inside fiber by convergence drawing have enabled detection of local impedance change with electrical reflectometry. We have demonstrated that these fibers can detect temperature and pressure change with high spatial resolution. We have also explored the possibility of using polymer optical fiber in a Raman scattering based distributed temperature sensing system. Stokes and Anti-Stokes signals of a PMMA fiber illuminated by a 532 nm pulsed laser was recorded, and the ratio was used to indicate local temperature change. We have also developed a unique way to fabricate porous polymer by thermal drawing polymer materials with controlled water content in the polymer. The porous fibers were loaded with a fluorescent dye, and its release in tissue phantoms and murine tumors was observed. The work has broadened the scope of multi-material, multi-functional fiber and may shed light on the development of novel smart textile devices.

Multi-Material Fiber Fabrication and Applications in Distributed Sensing

Li Yu

GENERAL AUDIENCE ABSTRACT

In recent years smart textiles and wearable gadgets have already changed the way we live. There has been increasing industrial interest to develop novel flexible, stretchable devices that can interact with human and the environment. Thermal drawing technique originally invented for manufacturing telecommunication optical fiber has been used by researchers to fabricate fibers with more functionality. In this work, we report the progress made on the fabrication of multi-material fiber. Soft polymer fibers capable of measuring temperature and pressure were designed and made by the thermal drawing technique. Submillimeter fibers with thin copper electrodes have shown potential to be readily embedded in a smart fabric to provide 1D information in one direction or woven into a 2D pattern for area monitoring. We have also explored another temperature measurement scheme using polymer optical fibers with a pulsed laser. Compared with the electronic fibers, it is less susceptible to electrical noise and more robust. Lastly, we have shown a unique way to generate porosity in thermally drawn polymer fibers. The elongated pores in the fibers come from water escaping the fiber during the fabrication process. The three aspects of the project expand the scope of multi-material, multi-functional fiber and can shed light on the future development of electronic textile devices.

Acknowledgements

First of all, I would like to express my deepest gratitude to my advisor, Dr. Anbo Wang, for his professional guidance, enormous encouragements, and tremendous help. He taught me a great deal about scientific research and life in general. Without his guidance and persistent help, my research progress in this subject and this dissertation would not have been possible.

Very special thanks go to Dr. Xiaoting Jia for her continuous support on this project. I would like to thank her for sharing with us her knowledge and expertise, and for her help and confidence. I would like to extend my gratitude to other members of my Ph.D. advisory committee, Dr. Yizhen Zhu, Dr. Luke Lester, Dr. Gary Pickrell and Dr. Yong Xu for their help, support, and comments. My sincere appreciation also goes to Dr. Yuanyuan Guo for teaching me the fiber drawing technique and offering helpful suggestions. I also would like to thank Dr. Daniel Homa and Dr. Rong Tong for all the productive discussions.

It has been an unforgettable experience to be a member in Center for Photonics Technology (CPT) during my graduate study. I would like to thank all the colleagues that I have worked with in CPT. They are all my sincere friends, and discussions with them are very beneficial.

Finally, I would like to thank my parents, who have always been supportive. They have always been there, and I appreciate all they have done for me.

Table of Contents

List of Figures

List of Tables

Chapter 1 Introduction

Distributed sensing is a technology that enables continuous measurement along the length of a continuous sensing element. Unlike traditional sensing systems that rely on multiple discreet sensors at different locations, distributed sensing system utilizes a single component such as optical fibers or electrical cables to sense the surrounding environment. It provides a cost-effective solution for applications that call for a large number of measurement points. Fiber or cable-based distributed sensing system also has the advantage of being flexible and having a small footprint, high spatial resolution and short response time.

One of the early examples of distributed measurement systems is using time-domain reflectometry to locate and characterize faults in electrical cables [1, 2]. Reflectometry on electrical cables has then been widely used in many areas. Coaxial cables have been grouted in rocks to monitor rock mass deformation or unstable slopes [3-5], and they have been installed underground to measure soil water content [6]. This method has also been applied to monitoring civil structures where embedded cables can detect hidden crack damages [7, 8]. The use of commercial coaxial cables that are not optimized for sensing purposes limits the scope they can be used. The cables' relative large diameter also poses a challenge for them to be woven into fabrics.

Another group of distributed sensing systems are based on fiber optic sensors. Silica optical fibers are submillimeter fused silica optical waveguides thermally drawn from large diameter silica rod called preforms. Although they are designed for high-speed telecommunication, silica optical fibers have also been used as sensors to measure temperature, strain, chemicals and more [9, 10]. Distributed fiber optical measurements have been realized by fiber Bragg grating (FBG) array [11, 12], Raman scattering based distributed temperature system (Raman DTS) [13], Brillouin optical time domain reflectometry/analysis (BOTDR and BOTDA) [14], frequency domain reflectometry (OFDR) [15], and many other methods. Their applications include downhole oil and gas monitoring, structure health monitoring, and pipeline leakage detection. Despite their higher transmission loss compared to silica optical fibers, polymer optical fibers have been widely used in short-distance data communication. Researchers have also used them

for fiber-based optical sensing. The same sensing principles mentioned above have been applied to the polymer optical fiber sensors with the focus on strain measurement due to the smaller Young's modulus and larger elongation limit of polymer materials compared to silica [16-18]. The measurement range of a polymer optical fiber distributed sensing system is mainly restricted by the transmission loss of the polymer optical fiber, which are two orders of magnitude higher than that of the silica fiber. For optic fiber based distributed sensors, the complexity and cost of most systems are the major hurdles that keep them from being used in consumer smart textile applications and products.

In recent years, the industrial interest in smart textiles and wearable electronics has attracted researchers to develop devices with various functionalities that can be integrated into fabrics [19, 20]. Electronic textiles have the advantage of being flexible, stretchable, and lightweight and they have been used in devices for display, sensing, energy harvest, and communication [21-24]. The fabrication techniques range from conventional deposition, coating on fiber-shaped substrates, to various spinning methods [25-28]. Among the numerous fiber-processing techniques, fiber thermal drawing technique initially designed for telecommunication optical fiber has been expanded to making various multi-material and multi-functional fiber structures [29-31]. Multilayer dielectric fibers with unique light-guiding properties were first reported in 1998 [32, 33]. Active fiber lasers utilizing the multilayer structure were soon developed, and fibers with electronic and optoelectronic functions have been fabricated by incorporating semiconductor materials in the fibers [34-36]. More advanced functional fibers, such as piezoelectric fibers, capacitive fibers, and surface-patterned fibers continue to emerge from the exploration of novel fiber materials and structures [37-40]. Some of the latest development includes diode-embedded fibers and stretchable fibers with a promising application in smart textiles [24, 41]. These functional fibers are not only used to make electronic textiles [24, 41-43], but also used as biomedical probes for neural recording [44, 45], nerve guidance scaffold [46, and specialized optical waveguide [47-50]. The thermal drawing process is also adapted to fabricate nanomaterials including nano-wires, nano-tubes, and nano-spheres [51-54]. One major advantage of the thermal drawing technique is achieving complex micro- and nano-scale feature size within a fiber from a macro-size preform. During the drawing process, the material and the

geometry can remain the same while the fiber's overall dimension is being reduced to sub-millimeter or smaller. Exceptions are the fabrication of nanosphere and reactive drawing where materials geometry and composition are intentionally altered during the drawing [55-56]. The technique also provides good production scalability that hundreds meter of fiber can be drawn from a single preform. With the breakthrough in understanding the fluid dynamics and rheology, a wide selection of functional materials can be co-drawn with traditional amorphous materials including glasses and thermoplastic polymers, which greatly increases the prospect of multi-material fibers research.

Multi-material fiber fabricated from thermal drawing for sensing application has been explored. Temperature and pressure are the most common parameters to be measured and multi-material-fiber based temperature and pressure sensors have been reported [36, 41, and 57]. The working principle of the heat-sensing fiber reported by Bayindir et al. is the temperature-dependent resistance change of the semiconducting glass inside the drawn fiber. Since the resistance of the fiber is proportional to the thermal excitation along its whole length, an array of the fiber was assembled to provide spatial information of the excitation and each fiber requires a separate circuit for the resistance measurement [36]. For the two pressure sensing fibers reported by Nguyen-Dang et al. and Qu et al., the location of the pressure was determined by electric contact and the maximum number points can be detected was limited to two [41, 57].

In this work, we have demonstrated the thermal drawing of multi-material fibers that can detect and localize temperature and pressure change by one-end connection with multi-point detection capability. Two copper electrodes inside the fiber form a parallel wire transmission line that responds to local perturbation. Frequency domain reflectometry was used to determine the location and extent of the change. We have combined the thermal drawing technique for multi-material fibers and reflectometry detection methods used in electrical cable distributed sensors to achieve both simplicity in detection and scalability for production. The result has opened new direction towards functional fiber and fabrics for pressure and temperature mapping.

The structure of the manuscript is as follows. The sensing principle of the multi-material electrode-embedded polymer fiber is described in the next chapter. We also present the detection

schemes to interrogate the sensing fiber in the same chapter. In chapter three, we focus on the thermal drawing technique and the fabrication process of the fibers used for temperature and pressure measurement. Testing procedures and fiber performance evaluation are described in chapter four. Chapter five highlights the second part of the project which focuses on optical distributed measurement of temperature with polymer optical fiber. The result of thermal drawing porous polymer fiber and its application is discussed in chapter six. Summary of the current progress is provided in the last chapter.

Chapter 2 Distributed Sensing Principle

2.1 Transmission Line Model

As discussed in the previous chapter, current polymer fiber-based sensing systems rely on measurement of changes in the total resistance or capacitance along the fiber, thus have limitations in their distributed sensing capabilities. In this chapter, we describe the fully-distributed sensing principle of the multi-material fibers designed and fabricated in this work.

When transmitting high-frequency signals, polymer fiber with a pair of electrodes can be treated as a transmission line, and a physical model is shown in **Figure 2-1 (a)** [58]. An infinitesimal segment of the fiber can be modeled as a lumped-element circuit, and the fiber can be viewed as a cascade of sections shown in the figure. Each segment is described by the following four per unit length quantities:

$$R = series\ resistance\ per\ unit\ length, in\ {}^{\Omega}/_{m}$$

$$L = series\ inductance\ per\ unit\ length, in\ {}^{H}/_{m}$$

$$G = shunt\ conductance\ per\ unit\ length, in\ {}^{S}/_{m}$$

$$C = shunt\ capacitance\ per\ unit\ length, in\ {}^{F}/_{m}$$

For a two-wire fiber whose electrodes are surrounded by dielectric materials, when the wire diameter is d, and the distance between the wires is D, the parameters are given as follows [58]:

$$\begin{aligned} R &= 2R_s/\pi d \\ L &= \mu/\pi \cdot \mathrm{acos}(D/d) \\ G &= \pi\sigma/\mathrm{acos}(D/d) \\ C &= \pi\epsilon/\mathrm{acos}(D/d) \end{aligned} \tag{2-1}$$

Where $R_s = \sqrt{\omega\mu/2\sigma_c}$ is the surface resistivity of the electrodes, and ϵ is the permittivity of the dielectric material. σ and σ_c are the conductivity of the dielectric material and the electrode

material. μ is the permeability constant, and ω is the angular frequency of the electromagnetic wave.

The characteristic impedance of the transmission line is the ratio of the amplitude of voltage and current of a single-frequency wave propagating along the line. It is determined by the geometry and the materials of the transmission line. For the two-wire system, it can be defined as:

$$Z_0 = \sqrt{R + j\omega L / G + j\omega C} \approx \sqrt{\frac{L}{C}} = \frac{1}{\pi}\sqrt{\frac{\mu}{\epsilon}} \cdot \operatorname{acosh}(D/d) \tag{2-2}$$

Assuming permeability is equal to the constant in the vacuum, an estimation of the impedance of a parallel wire transmission line is shown in **Figure 2-1 (b)**. The characteristic impedance of a typical parallel-wire transmission line is between 100 and 300 Ω. In most cases, the diameter of the electrodes d and permeability μ does not change. If at one point the distance between the electrodes D and the permittivity ε is different from a previous section, it would lead to a change of the local impedance. The discontinuity of the impedance will cause a partial reflection of an electric signal being transmitted, and the reflection coefficient is:

$$\rho = \frac{Z_1 - Z_0}{Z_1 + Z_0} \tag{2-3}$$

Where Z_0 is the original impedance, and Z_1 is the new impedance.

Equation 2.2 and 2.3 suggests that geometric or electrical change of the transmission line can induce reflection at the specific location. When the distance between the two wires increases or the dielectric material's permittivity decreases, the local impedance will increase, leading to a positive reflection. A negative reflection occurs when the distance decreases or the permittivity increases.

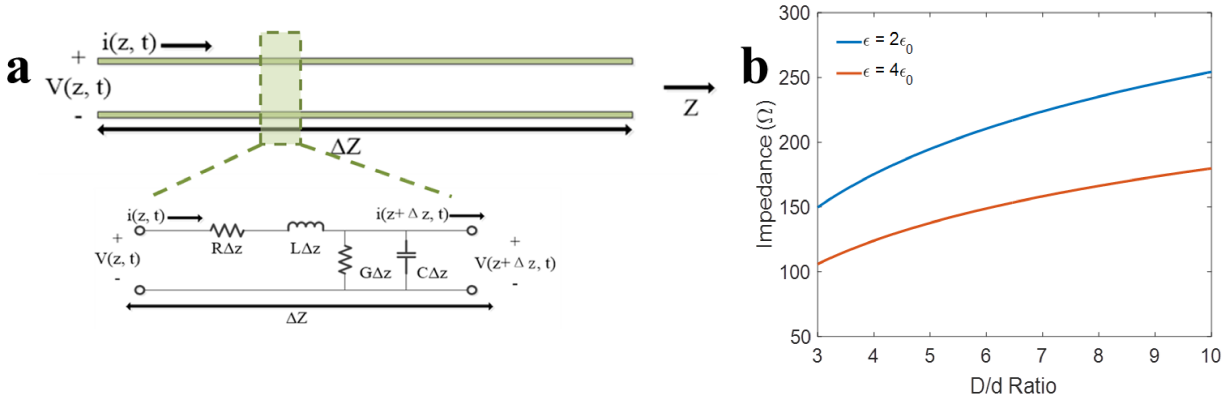

Figure 2-1 (a) Transmission line model of a two-electrode fiber (b) Calculated impedance of two-electrode fiber with different D/d ratio

Temperature and pressure are two common measurands, and polymer materials are intrinsically more sensitive to the change of temperature and pressure compared to fused silica. When polymers are heated, their relatively large thermal expansion will alter the geometric size, thus change the distance between the two electrodes. At the same time, some polymers' permittivity will also change which affects the impedance of the heated segment as well. Researchers have reported using commercial electrical cables to measure heat zones along the line [59]. By substituting coaxial cables with polymer fibers, the sensor size can be reduced. For this work, we have selected three polymers as potential material used in the temperature-sensing fibers. For pressure sensing, a hollow deformable structure similar to the fiber presented by Nguyen-Dang et al. [57] or a soft material between the electrodes can ensure a detectable distance reduction that leads to decrease of the local impedance [41]. **Figure 2-2** show the two pressure sensing scheme we proposed. We have pursured both directions, and the detailed fiber design are discussed in the next chapter.

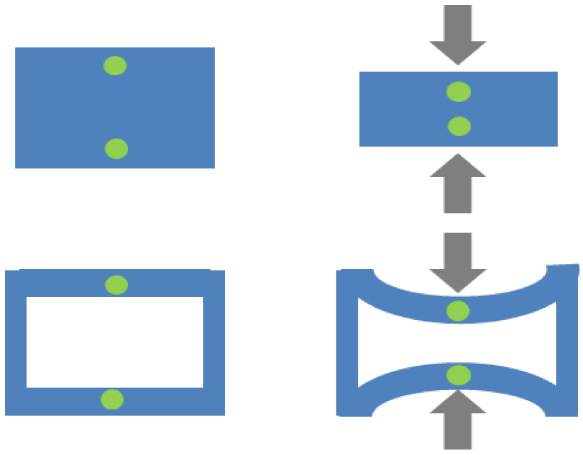

Figure 2-2 Illustration of two fiber structures proposed for pressure sensing

2.2 Detection Scheme

2.2.1 Time Domain Reflectometry

The localized change of impedance can be detected by Time Domain Reflectometry (TDR) and Frequency Domain Reflectometry (FDR). TDR has been widely used to evaluate discontinuities along a transmission line. In a typical TDR system, a step or pulse signal is sent down the transmission line under investigation, and the reflection is monitored by an oscilloscope [60]. Each time the signal encounters an impedance variation, a partial signal is reflected and captured by the oscilloscope. The change of the impedance discontinuity can be determined from the amplitude of the reflected signal using Equation 2-3. The position of the discontinuity can be calculated from the time that the pulse takes to return with the following equation:

$$t_i = {2z_i\sqrt{\epsilon_r}}/{c} = {2z_i}/{(VF \cdot c)} \tag{2-4}$$

Where VF is the velocity factor of the transmission line (usually ranging from 0.5 to 1 based on the permittivity of the material), and c is the speed of light in vacuum. The pulse width determines the spatial resolution of a TDR system, therefore a sub-nanosecond pulse is usually used to achieve high resolution. **Figure 2-3** is an illustration of a simple TDR system.

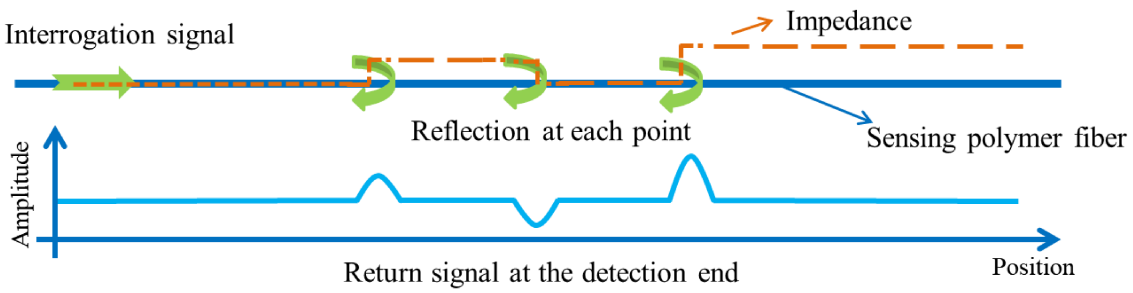

Figure 2-3 Illustration of the distributed sensing principle for a TDR system

2.2.2 Frequency Domain Reflectometry

There are several types of FDR systems, and we focus our discussion on the Phase-Detection Frequency Domain Reflectometry (PD-FDR). In PD-FDR, a set of stepped-frequency sine waves are launched to the transmission line. The return signal at each step contains amplitude and phase information. The frequency response is used in an inverse Fourier Transform to acquire the time-domain information [61]. The reconstructed signal is similar to the direct measured response from TDR. The mathematical derivation is given in several references. Here we use the formulae presented by Huang et al. [62]. Consider a waveform given by:

$$V_o = A \cdot \exp\{j(\omega t + \varphi)\} \tag{2.4}$$

Where t is the time; V_0 is the voltage; A is the amplitude; φ is the initial phase; ω is the angular frequency of the particular step. Multiple reflections occur at different points, and the total voltage of the reflection wave by discontinuities is the sum of the individual reflection:

$$V_{total} = \sum_{i=1}^{N} V_{o,i}(t, z_i) \tag{2-5}$$

Where N denotes the number of reflectors, z_i represents the location of the i-th reflector, and the voltage component is given by:

$$V_{o,i}(t, z_i) = \Gamma_i A \cdot \exp\{j\left[\omega\left(t - {2z_i\sqrt{\epsilon_r}}/{c}\right) + \varphi\right]\} \tag{2-6}$$

Where Γ_i denotes the reflection coefficient of the i-th reflector; c denotes the speed of light in vacuum, and ϵ_r is the relative permittivity. The transfer function at a specific frequency is then given by:

$$H(\omega) = {}^{V_{total}}/_{V_o} = \sum_{i=1}^{N} \Gamma_i \cdot \exp[j({}^{-2z_i\sqrt{\epsilon_r}\omega}/_{c})] \quad (2\text{-}7)$$

By sweeping the frequency from ω_{min} to ω_{max}, the impulse response of the system can be calculated by an inverse Fourier transform.

$$h(t) = \frac{1}{2\pi}\int_{\omega_{min}}^{\omega_{max}} H(\omega) \cdot \exp(j\omega t)\, d\omega = \sum_{i=1}^{N} \Gamma_i \cdot sinc[(\omega_{max} - \omega_{min})(t - \tau_i)] \quad (2\text{-}8)$$

Where $\tau_i = {}^{2z_i\sqrt{\epsilon_r}}/_{c}$ is the delay of the signal of the i-th reflector. From Equation 2-8, we can see that the amplitude of each sinc function is proportional to the reflection coefficient of the reflection point and the location of the reflection can be calculated from the delay time. The time-domain reflection signal after transformation is very similar to the direct TDR signal shown in **Figure 2-3**. The frequency range, step value, and the window function dictate the spatial resolution of the system [63]. For the FDR system used in this work, a Vector Network Analyzer (VNA) is used to perform the frequency scan and the subsequent inverse Fourier Transform, and post-processing is carried out in Matlab. The sensing performance is heavily dependent on the VNA specification and setting. The detailed discussion is in chapter 5.

Chapter 3 Multi-material Fiber Fabrication

3.1 Thermal Drawing Technique

The thermal drawing process is well known from the telecommunication fused-silica optical fiber production. Polymer optical fibers are manufactured by extrusion or thermal drawing [64]. Although it is possible to fabricate multi-material polymer fibers using extrusion methods or 3D printing [65], we have limited the scope of our work to the thermal drawing technique. The basic principle of thermal drawing multi-material fibers has been established and discussed in detail [29-31, 41]. The process involves two separate steps. A macroscopic preform resembles the final fiber geometry and composition is first made from functional materials including polymers, glass, metals, nano-materials or semiconductors. When the preform is heated in a furnace, rigid thermoplastics and glasses with a decreased viscosity at a temperature above their glass transition temperature are drawn into fibers with a reduced cross-sectional dimension. We will discuss the two steps in detail in the next few paragraphs.

For a silica optical fiber preform, the diameter is in the range of 20-300 mm, and the length is around 1 m [66]. Industrial fabrication of ultra-high purity and uniformity silica preforms usually start with chemical vapor deposition methods including modified chemical vapor deposition (MCVD), plasma chemical vapor deposition (PCVD), outside vapor deposition (OVD), and vapor axial deposition (VAD). Gaseous precursors such as $SiCl_4$ are delivered to a substrate, and chemical reaction of the vapor generates high-quality SiO_2 which is deposited on the substrate. After soot deposition and sintering, the layer becomes dense and optically transparent. There are additional steps such as tube collapsing, sealing and post-processing at high temperatures depending on the methods used. Once the preform is made, due to the brittleness of silica glass, direct machining of the preform is possible but usually inconvenient [67, 68]. Microstructure silica optical fiber relies on stacking of capillary tubes or solid rods to the desired pattern and heat fusing the assembly into a solid preform before drawing [66].

Thermoplastic polymer preform fabrication is more versatile thanks to their better machinability and lower process temperature. Some of the methods are: 1. drilling and milling of plastic bars

and rods for patterned surface and hollow channels; 2. hot press of different materials in vacuum oven slightly above their glass transition temperature for consolidation; 3. thin-film rolling around a mandrel followed by consolidation to generate a circular layer; 4. additive manufacturing of preform from filaments [69,70]. The preform preparation sometimes involves incorporation of functional materials including electrodes, liquid polymer solution, liquid metal, and photodiodes into the preform as well [24, 41, 71].

Once the preform is made, it is heated in a vertical furnace for drawing. For thermal drawing polymer preforms in our lab, the top end of the preform is usually fixed while the bottom is attached to a weight during the initial heating. When the middle section of the preform inside the furnace is softened after being heated beyond the material's glass transition temperature, the decreased viscosity permits deformation of the preform and initializes the drawing. The middle section becomes thinner as the bottom part exits the furnace to be collected by a capstan. The top end of the preform is then set to move down at a much slower speed to feed the preform to the furnace to continue the drawing. By adjusting the feed rate, the capstan rate, and the furnace temperature, the final fiber diameter can be controlled. The ratio between the size of the preform and the fiber is called draw-down-ratio (DDR), and the following general relations are valid:

$$Feed\ rate = Capstan\ rate / DDR^2$$

$$Fiber\ length = Preform\ draw\ length \times DDR^2 \quad (3\text{-}1)$$

Usually, the preform diameter is around 20 mm, and the fiber diameter is less than 1 mm. Assuming DDR is 50, a preform with 10 cm usable length can readily be drawn into 250 m of fiber, which provides a much higher yield than single device fabrication [72, 73].

Photo of one of the fiber draw towers in CPT is shown in **Figure 3-1 (a)**. The furnace, the feeding stage, and the capstan are shown in the figure. The tube furnace from Mellen has three temperature zones. The middle zone temperature is the highest of the three and is set to be higher than the polymer's glass transition temperature. A laser micrometer (Laserlinc) and a tension gauge are used to measure the fiber diameter and the draw tension. The preform feed rate and the capstan rate are controlled manually by motor controllers. A Labview program (offered by the

vendor) is used to control the furnace temperature and to process fiber diameter and tension information.

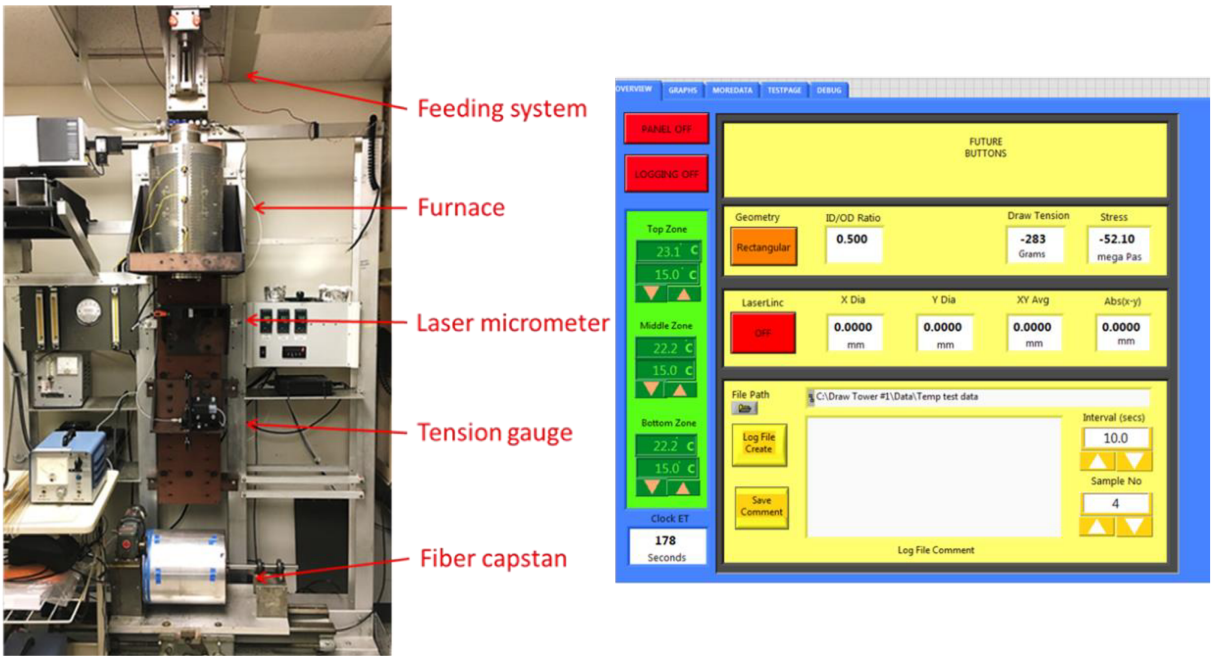

Figure 3-1(a) Fiber draw tower in Center for Photonics Technology, Virginia Tech (b) Control interface for the draw tower system

The key to successfully drawing is to identify materials that can be co-drawn with the supporting amorphous materials. The supporting material needs to be able to continuously and controllably deform while supporting the drawn stress to allow stable drawing. Thermoplastic polymer used in this work, low-temperature glass and silica are all good candidates but requires different draw temperatures. Additional macro-size materials such as semi-crystalline polymer materials placed in a preform should flow at the drawing temperature, and crystalline material such as metal should have a melting temperature below the draw temperature. Small size devices like photodiode and high-melting-temperature metal electrodes whose size is the final dimension can be co-drawn with the supporting material with special care [24]. We will discuss the co-drawing of electrodes in the next paragraph.

Electrodes have previously been used to as electrical probes to detect neuron signals in mice brain, and in fibers with semiconductor devices and capacitors to provide electrical connections

to the devices along the fiber [37, 38, 40-45]. In these cases, the electrical signal is well below the microwave frequency range thus electrode materials can be a low-temperature metal alloy such as BiSn or conductive polymer like carbon black-doped Polycarbonate (CPC). The conductive materials surrounded by amorphous materials in the preform would become either viscous or molten and turn into thin electrodes inside the fibers during drawing. The challenge of this method is that the metal/alloy has to have a slightly lower melting temperature than the drawing temperature. If the temperature difference between the two is too large and the drawing tension is too small, the surface tension of the metal/alloy will force the molten liquid into droplets.

For the distributed sensing fiber we have fabricated, low impedance of the electrode would ensure longer detection range, thus copper electrodes are used instead, which requires the convergence drawing method reported by Rein et al. [24]. For convergence drawing shown in **Figure 3-2**, metal wires are passed through the channels inside the preform. As the softened preform being drawn into fiber, the channel size decreases and converges on the metal wires. The distance between the electrodes pair is determined by the location of the channels in the preform. This method provides a way to embed high-melting-temperature metal electrodes in the fiber, providing high conductive electrical connection. It also poses little temperature constraint of the material used as electrodes. Copper wires are used in all the experiments included in this work.

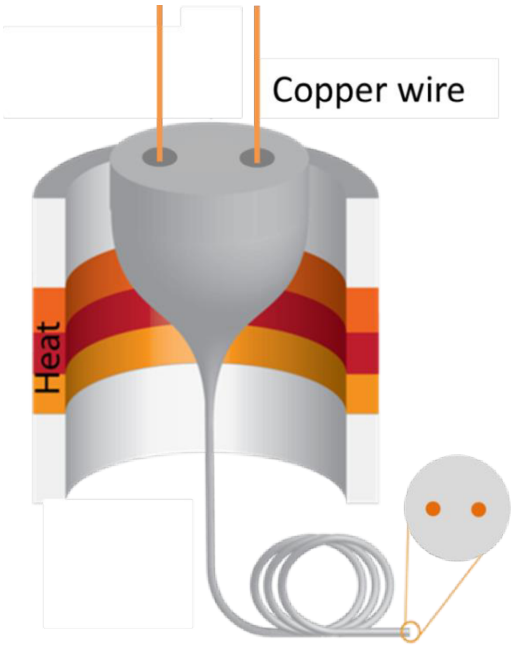

Figure 3-2 Illustration of convergence drawing of two copper wires inside a polymer preform

3.2 Material Selection

Table 3-1 lists thermoplastic polymers that we have used for this project. The glass transition temperature is the range of temperatures where amorphous materials experience gradual and reversible transition from hard "glassy" state into a viscous state. The thermal drawing temperature is always higher than the glass transition temperature so the polymer material can deform. The glass transition temperature data are retrieved from the Handbook of Polymers by Wypych [74]. The last three polymers, LDPE, HDPE, and PVDF are semi-crystalline polymers. They have partly-ordered regions with a typical size of few micrometers. They have melting temperatures much higher than their glass transition temperatures and their drawing temperature has to exceed the melting temperature to counter the intermolecular forces. Also because their viscosity rapidly changes near the melting temperature, stable drawing the materials by themselves sometimes is difficult. Co-drawing with amorphous thermoplastics is preferred.

Polymer	Glass transition temperature [74]	Draw temperature	Comments
Poly (methyl methacrylate)	82~105 ℃	235~250 ℃	
Polycarbonate	134~158 ℃	270~290 ℃	
Polyetherimide	209~249 ℃	320~360 ℃	
Cyclic olefin copolymer	62~177 ℃	270~290 ℃	
Poly (vinylidene fluoride)	-29~-57 ℃	270~290 ℃	Difficult to draw alone
Polyethylene, low density	-103~ -133 ℃	160~180 ℃	Difficult to draw alone
Polyethylene, high density	-118~-133 ℃	220~250 ℃	Can't be to draw alone

Table 3-1Thermoplastic polymer materials used in this work

Temperature changes both the distance between the two electrodes inside the polymer and permittivity of the materials. Larger volume change will induce more substantial impedance change which leads to a stronger reflection signal. Therefore, to increase polymer fibers' sensitivity, the coefficient of thermal expansion of common thermoplastics is examined, and we have found that low-density polyethylene (LDPE) has a large thermal expansion coefficient between $1\sim5.1\times10^{-4}K^{-1}$ [74]. The data for the permittivity change with temperature is less studied, but we have found publications reporting that LDPE has a negative relationship between temperature and permittivity [59, 75]. This property would further increase fiber local impedance of a LDPE fiber when the fiber is heated. Poly (methyl methacrylate) (PMMA) thin films have shown to have relative large response to temperature, and that can be further enhanced by dopant [76, 77]. Poly (viny1idene fluoride) (PVDF) is a piezoelectric polymer widely used as a sensing material which also has temperature dependence of its permittivity [78]. Therefore, the three materials were chosen to make preforms for the temperature sensing polymer fiber.

Shape deformation is the key for pressure sensing thus two approaches have been proposed: a hollow structure that deforms under pressure or using polymer material with low Young's modulus in a solid structure. **Table 3-2** lists Young's modulus of common thermoplastics, and it shows that LDPE has the lowest value. Therefore it was chosen to be used in the hollow fiber

structure. For a solid fiber structure design, on the one hand, common thermoplastics such as PMMA, Polystyrene (PS), and Polycarbonate (PC) all have Young's modulus larger than 1 GPa, making it very challenging to detect pressure smaller than 1 MPa. On the other hand, though offering good elasticity and having lower tensile modulus under 100 MPa, elastomers usually are thermosetting polymers that do not soften by heating after initial curing. This prevents us from using them in the thermal drawing process. Thermoplastic elastomers (TPEs) are made from various copolymers combining thermoplastics and elastomers. They can be stretched or pressed and return to its original shape like elastomers, and they can be softened and processed repeatedly like thermoplastics. The most common manufacturing methods for TPEs are extrusion and injection molding but we have successfully used them to fabricate pressure sensing fiber through the thermal drawing process. The TPEs used in this work are Versaflex CL2242 and CL2250 from Polyone. They are SEBS (styrene and ethylene/butylene) TPEs and have a 100% tensile stress of 1.05 MPa and 1.52 MPa. The exact pressure-compression relationship is not provided by the vendor. The TPEs were provided in the form of 1 mm thickness sheets and were subsequently pressed into desired shapes in vacuum at 180 ºC. We have also tried TPEs used by Qu et al. in reference [41]. The first two are G1657 and G1652 from Kraton Performance Polymers, which also belong to the SEBS copolymer. The third one is Wacker's SLM TPSE 345, which is a siloxane-based copolymer. These three TPEs come in the form of pellets and are pressed into plates before use.

Polymer	Young's modulus/(GPa)
Polyethylene, low density	0.14-0.3
Polyethylene, high density	0.7-1.4
Polypropylene	1.1-2
Poly(methyl methacrylate)	2.5-3.3
Polycarbonate	2.1-2.4
Polystyrene	2.4-3.2
Acrylonitrile-butadiene-styrene Medium IS	2-2.8
Acrylonitrile-butadiene-styrene High IS	1.6-2.5

Table 3-2 Young's modulus of common thermoplastics [79, pp 443]

3.3 Fabrication of Temperature Sensing Fiber

One inch diameter PMMA rods (US plastics) were used for making the PMMA fiber preforms. Polymer materials such as PMMA and PC are always degassed in a heated vacuum oven for at least two weeks before use to remove water residual. The copper wire had a diameter of 0.005 inch (McMaster Carr), and the two hollow channels were drilled with a 0.125-inch drill bit. To match the diameter of the electrodes and the hollow channel, the draw-down-ratio was set to be 25 (0.125/0.005), and the final fiber diameter would be 1 mm. The two copper wires were fed through the drilled hollow channel from the side, and the wire spools were fixed on the preform holder. The wire feeding was passive, meaning that drawn fiber drags the wires with it during the drawing. The preform was drawn at temperature 140/240/100 ℃ (top/middle/bottom temperatures for the three-zone furnace). **Figure 3-3** shows the close view of how the preform and wire spools were mounted on the preform holder and the preform after the drawing. As shown in the figure, the copper wires are passed through two aluminum guiding tubes attached to the brown preform holder before entering the hollow channels drilled inside the preform. The hollow channels and the copper wires are also visible in the photo showing the preform after drawing. **Figure 3-4 (a)** and **(b)** show photo of the fiber spool and the cross section of the fiber under optical microscope.

Direct drawing PVDF was proved to be difficult after preform broke during the initial heating period. The modified PVDF preform has a PC cladding because PVDF is a semi-crystalline polymer whose viscosity drops fast after reaching the melting temperature. A cladding layer maintains the shape of the preform when it is heated and prevents the fiber from breaking. Two hollow channels were drilled near the surface of a 0.75 inch PVDF rod, and the rod was then inserted into a 0.75 by 1 inch PC tube. The preform was consolidated in a vacuum oven at 180 ℃ and then thermally drawn at 150/270/110 ℃. The PC cladding and the center PVDF can be identified from the fiber cross-section image shown in **Figure 3-4 (c).**

The LDPE preforms were made from LDPE square bars (McMaster Carr). Two 0.125 inch diameter hollow channels were drilled in a 1.25 by 1 inch LDPE bar for the copper wire to pass

through. Because both the glass transmission temperature and the melting point is low, the preform was drawn at 130/165/80 ºC. Even though LDPE is also a semi-crystalline polymer, we were able to draw the fiber without an outer thermoplastic cladding. The three polymer fibers and cross sections are shown in **Figure 3-4**.

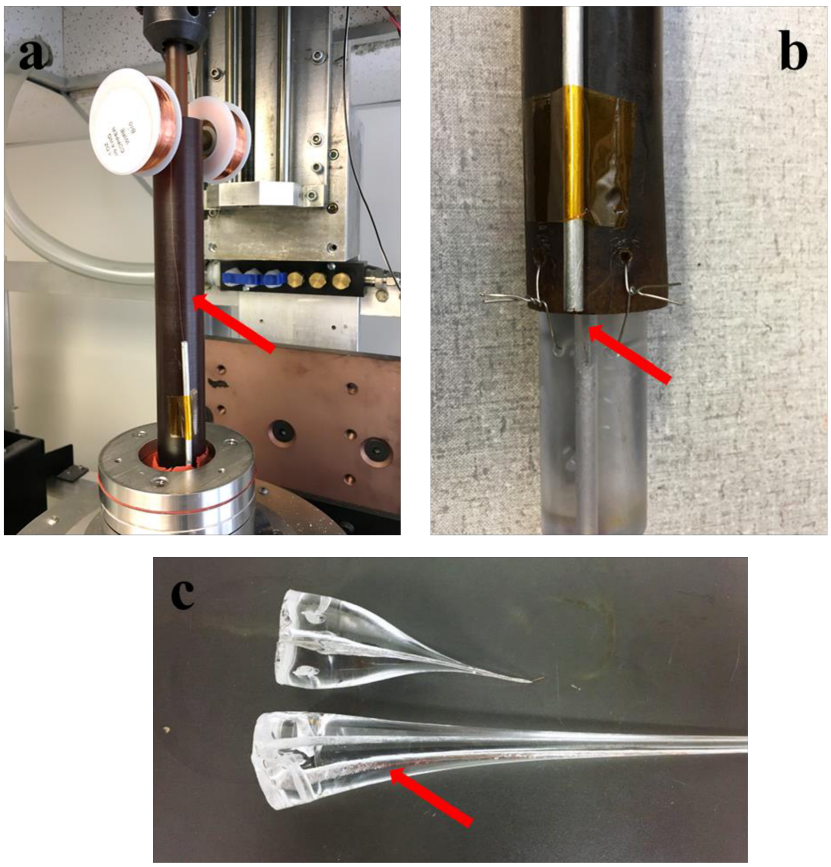

Figure 3-3 (a) Photo showing copper wires entering the aluminum guiding tubes attached to the preform holder (b) Photo showing copper wires exiting the guiding tube and going into the hollow channels of the preform (c) Photo of the preform used for the drawing (red arrow indicates the position of the copper wires)

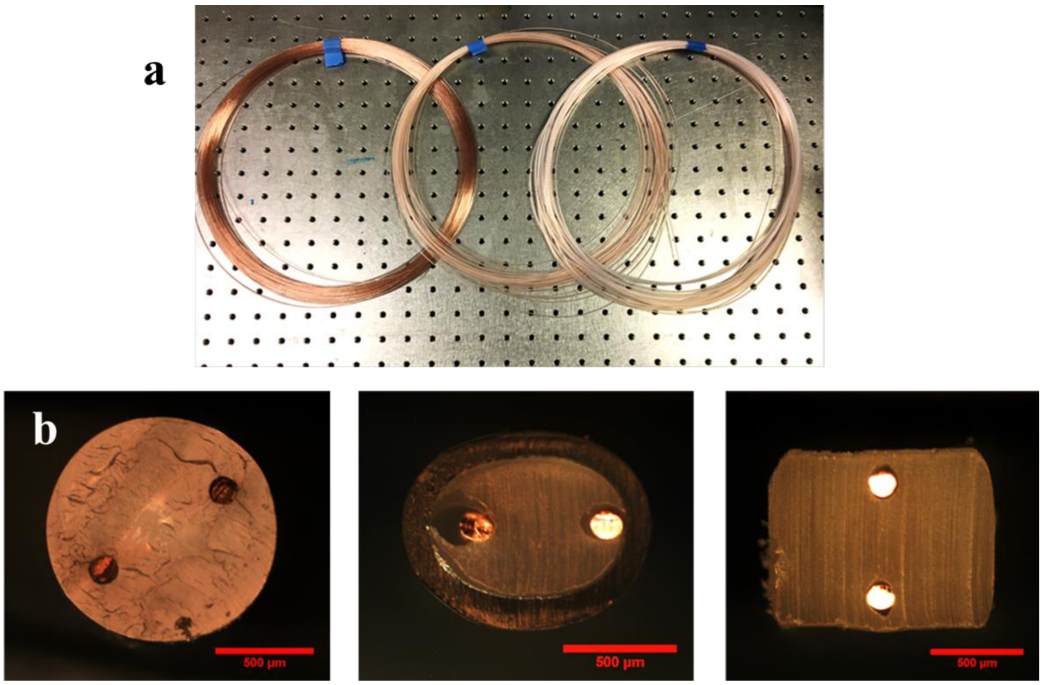

Figure 3-4 (a) spools of the three fibers with 125 µm copper electrodes inside (b) Optical microscope image of the fibers from left to right: PMMA fiber, PC/PVDF fiber and LDPE fiber, scale bar is 500 µm

3.4 Fabrication of Pressure Sensing Fiber

3.4.1 Hollow Structure Fiber

In order to predict the extent of deformation under pressure for a hollow structure fiber, computer simulations were carried out with software Comsol Multiphysics. The original design was a rectangular fiber with a central hollow cavity and two copper electrodes on the side. The simulated fiber size is 1.25 mm by 1 mm, and the wall thickness is 0.3 mm. The value is chosen to be so the fiber can be drawn from a 1.25 by 1 inch LDPE block and 125 µm copper wires. It is expected that when hydrostatic pressure is applied to the fiber, the longer sides of the rectangular fiber will bend inward, reducing the distance between the two electrodes. The simulation result of such fiber made with PC and LDPE is given in **Figure 3-5** (PC was chosen for pressure response comparison). The results show that LDPE indeed provides a larger deformation (3.8 µm compared to 0.4 µm) due to its smaller Young's modulus. We have also noticed that the thickness of the longer side of the rectangular largely determines the pressure sensitivity thus

improvement of the structure was made to reduce the its thickness while keeping the original dimension of the middle region where the electrodes are. Nearly ten-fold of sensitivity increased was achieved by reducing the thickness from 300 μm to 125 μm and another three-fold increase could be expected if the thickness was further reduced to 100 μm. The comparison is also shown in **Figure 3-5**.

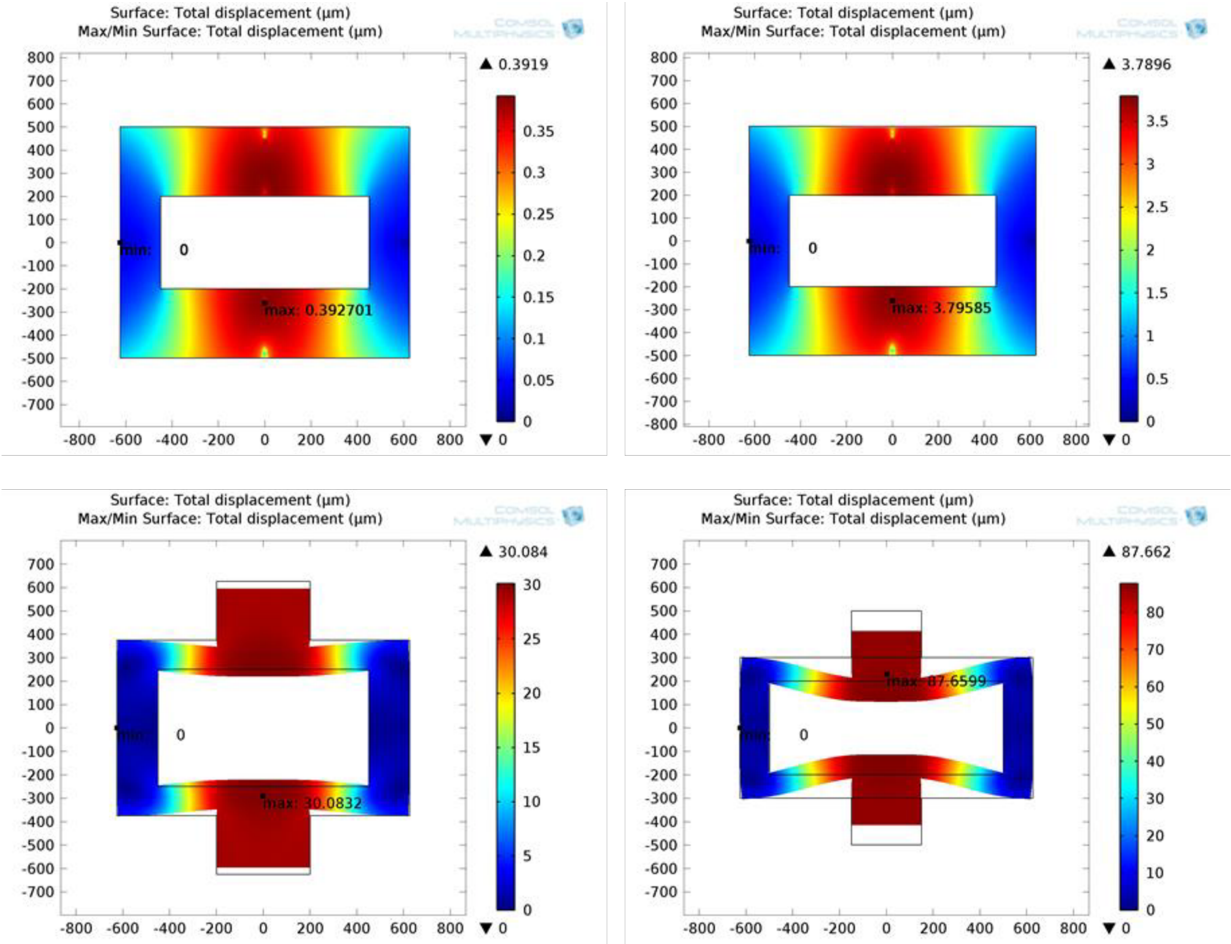

Figure 3-5 Simulation of polymer fiber deformation under 0.5 MPa: PC fiber (top left); rectangular PE fiber (top right); 125 μm wall PE fiber (lower left) and 100 μm wall PE fiber (lower right). Electrodes are omitted in the simulation. Number in the figures indicated deformation

Preform matching the 125 μm wall PE fiber shown in **Figure 3-5 (c)** with a projected draw-down-ratio of 25 was machined from a 1.25 by 1.25 inch LDPE bar by first cutting the four corners followed by milling away the center on a CNC machine. The preform was thermally drawn in the furnace, but unfortunately, due to the thin walls and large cavity size, the preform

collapsed during the drawing and the geometric shape could not be maintained, as shown in **Figure 3-6 (a)**. Taking a step back, we machined the rectangular preform a 1.25 by 1 inch LDPE bar. Several attempts were made to draw the hollow polymer fibers, and **Figure 3-6 (b)** and **(c)** show the results from the drawing. By comparing the preform photo and the fiber cross section, it is clear that the wall of the cavity was stretched thinner than the design and the cavity became larger instead. Unlike PC and PMMA, LDPE's semi-crystal nature gives a narrow softening/melting temperature region between 160 and 180 ℃. It is possible to draw the solid LDPE fiber with copper electrodes, but the hollow structure is more challenging. When the drawing temperature is lower, the fiber tends to break while slightly higher temperature decrease the polymer's viscosity too much causing copper wires to escape from the fiber. Low viscosity of the polymer also allowed the copper wire in the walls to protrude and deformed the fiber. Therefore, we have focused on drawing fibers with solid structures later on.

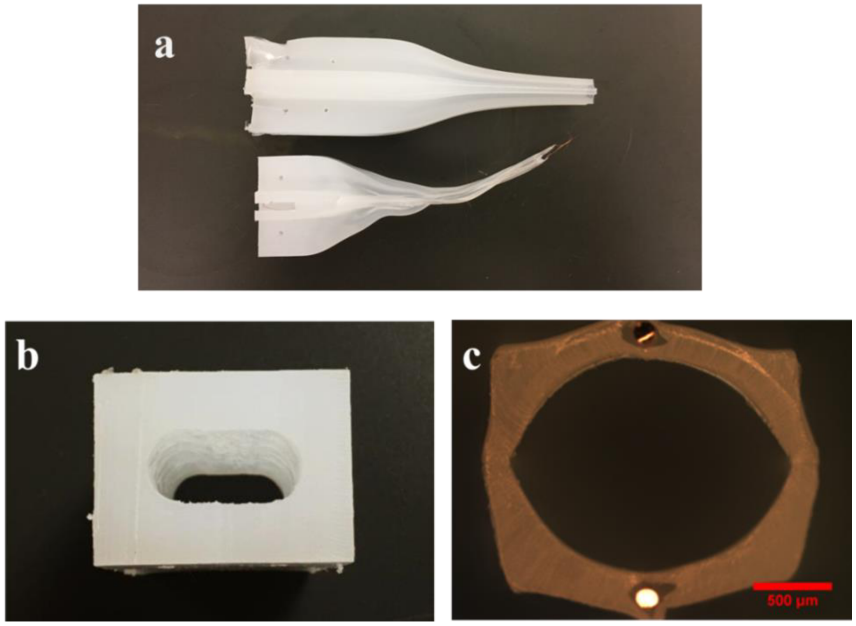

Figure 3-6 (a) The preform after failed thermal drawing (b) The 1 by 1.25 inch LDPE preform before drawing (c) Optical microscopic photo of the cross section of the LDPE fiber drawn

3.4.2 Solid Structure Fiber

Unlike the hollow structure fibers that respond to hydrostatic pressure, the solid structure fibers are used for measuring lateral pressure that reduces the distance between the two electrodes.

Theoretically, a hydrostatic pressure could cause the fiber to shrink and change the distance between the electrodes, but the necessary pressure would be very large. Several iterations of fiber design were conducted before the optimum structure was determined.

The pressed CL2250 TPE block is shown in **Figure 3-7 (a)**. After several drawing attempts, we have determined that none of the TPE blocks can be directly drawn. While TPE's viscosity decreased at elevated temperature, the elastomer's mechanical strength also decreases causing the preform to break during the bait off. PMMA plates were then added to both sides of the TPE blocks to help with the draw. Although the TPE would be soft and prone to break, the PMMA would retain enough mechanical strength to prevent the preform from breaking. Two grooves were milled on the inner surface of the PMMA plates for the copper electrodes, and the plates were attached to the center TPE block. The assembly was then heated in a vacuum oven at 140 ºC for the PMMA to adhere to the TPE. The photo of assembled preform is given in **Figure 3-7 (b)**. Two TPEs, CL2242 and CL2250 were successfully co-drawn with PMMA and 125 μm copper electrodes inside. However, the center TPE layer was stretched horizontally by the two PMMA layers on the side. The reason is that PMMA requires a drawing temperature of 240 ºC and both TPEs' softening temperature is below 220 ºC. In order to co-draw the two materials, 240 ºC has to be used yet the high temperature has caused the TPE to become too soft and split.

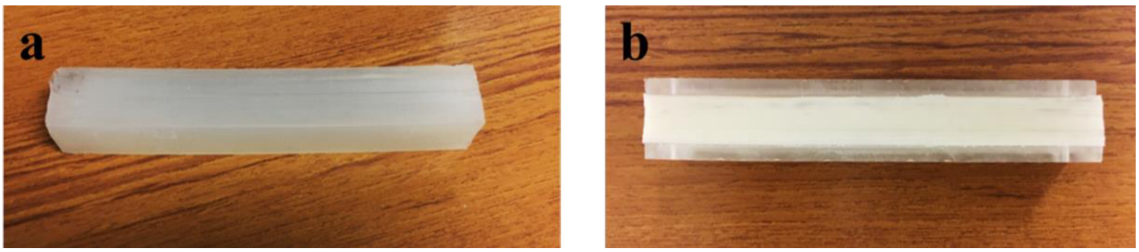

Figure 3-7 (a) TPE block from hot press, (b) TPE/PMMA preform with hollow channel in the PMMA

After experimenting, it was discovered that adding another layer of PMMA plate in the middle of the TPE would slow down the split. New preforms were made from two 4.5 mm PMMA plates with 2.5 mm grooves milled on the inner surface, two 4 mm TPE plates and a center PMMA plate. The five-layer preform and the drawn fiber are shown in **Figure 3-8 (a)** and **(b)**. Although the general shape is preserved, there are a few issues with the fiber. First, the copper wire enlarges the grooves by protruding to the soft TPE region thus leaving voids between the

electrodes and the polymer in the final fiber. Second, since the grooves were machined by a square end mill, the contour of the groove did not match well with the electrode. A modification was made to contain copper wire inside the outer PMMA plate so that it does not enter the TPE region during drawing. Also, the grooves were milled using a ball-end mill bit to match the curvature of the electrodes. The preform structure is given as follows: a 1 inch by 3 mm PMMA plate is sandwiched by two 1 inch by 4 mm TPE plates on the outside. Two 1 inch by 3 mm PMMA is pressed against each other on each side of the TPE plates with a 2 mm diameter groove in between for the copper electrodes. The whole assembly of seven layers was consolidated in a vacuum oven for 30 minutes at 140 ºC. With the use of 80 µm copper wires as electrodes, the projected draw-down-ratio was 25, and the preform was drawn at 140/245/100 ºC. The final fiber is shown in **Figure 3-8 (c)** and **(d)**. The first several meters of fiber showed good structural integrity. After that, the TPE will still gradually being pulled away, and the fiber structure is no longer maintained. The comparison is also shown in the figures. In order to solve the splitting issue, we have further improved the fiber design by adding a full cladding.

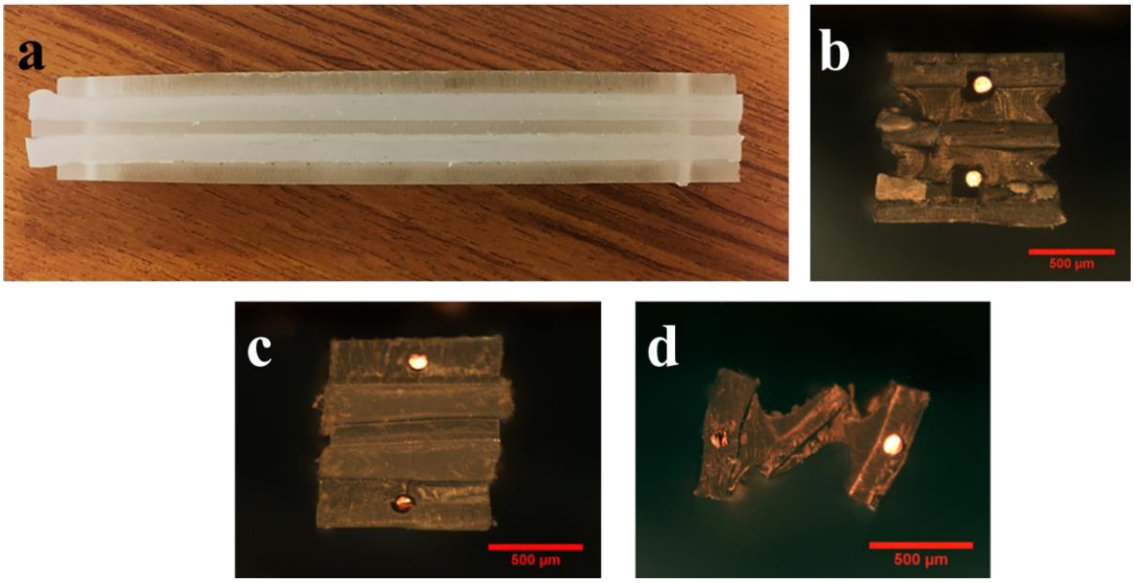

Figure 3-8 (a) five-layer TPE/PMMA preform with center plate, (b) fiber drawn from the preform, (c) fiber drawn with modified, seven-layer fiber drawn from modified preform and (d) split fiber after several meter

A four-side cladding, different from the previous two-side cladding, was added to the fiber design to ensure stable drawing without splitting. The cladding would act as a shell to help TPE maintain its geometry during the thermal drawing and would increase the overall strength. Both PC and PMMA and excellent thermoplastic polymers for thermal drawing and they are selected to be used as the cladding material. There are three possible ways to add a cladding to the original square core. First method is inserting the core preform directly into a square tube with a matching size. The advantage of the method is that the cladding's shape is well-defined and the disadvantage is that the core preform and the tube cladding may not fit perfectly. The second method is to use four plates around the core preform and consolidate in a heated vacuum oven so that each plate adheres to the other plates as well as the core. This method ensures a better size match as the size of the plate can be more readily adjusted to the core preform. The preforms made with the two methods are shown in **Figure 3-9 (a)**. We were able to draw the preform made with the first method, but the possibility of generating a gap between the tube and the core preform let us eventually abandoned the approach. The preform made with the second method failed to hold the structure during the drawing as the consolidation of the four plates around the core preform was not strong enough. Therefore we move on to the last method which is tightly wrapping thin polymer film around the core followed by pressing the layered polymer into a solid cladding in a vacuum oven. When the film is relatively thin, such as the 75 μm PC film and the 125 μm PMMA film used in this work, though the wrapping creates a rounded shape, the assembly can be pressed back to a square shape with the help of a C-shape metal mold. Both films were used to make the cladding, and the preforms were successfully drawn into fibers.

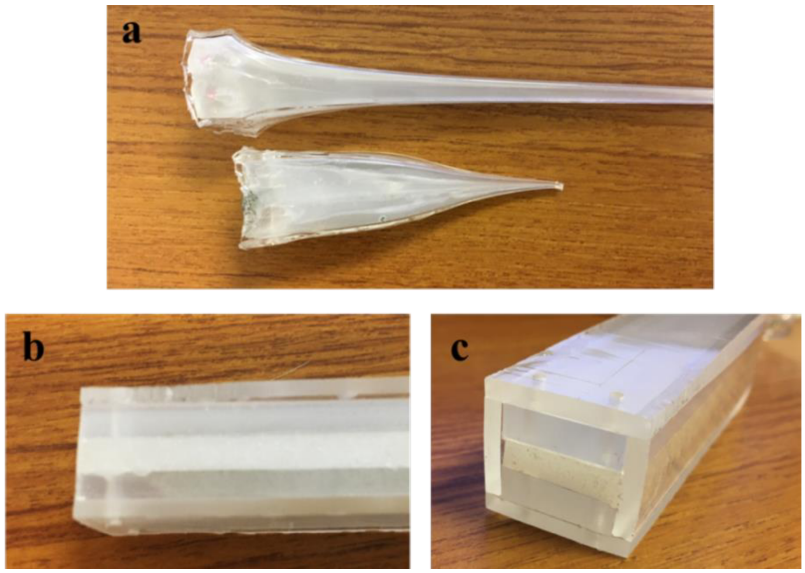

Figure 3-9 (a) Preform made from inserting the core preform into a 7/8 by 1 inch PMMA square tube (Photos are taken after thermal drawing thus the preform show deformation from the heating), (b) and (c) Preform made from consolidating four PMMA plates around the core preform (Photos are taken after thermal drawing thus the preform show deformation from the heating)

Although the cladding significantly improves the drawing outcome, the hard plastic layer would prohibit the fiber to deform under lateral pressure. Therefore, the cladding has to be etched away after the drawing. To prevent the organic solvent to damage the core part of the fiber, a very thin layer (~1 mm) of LDPE or PVDF film between the cladding and the core structure was wrapped to the core first. The LDPE was used with PMMA film while the PVDF was used with PC films based on their respective drawing temperatures. The organic solvent can be Dichloromethane (DCM), chloroform or toluene. The schematics of the fiber structure and a photo of a PC/PVDF/TPE preform are shown in **Figure 3-10**.

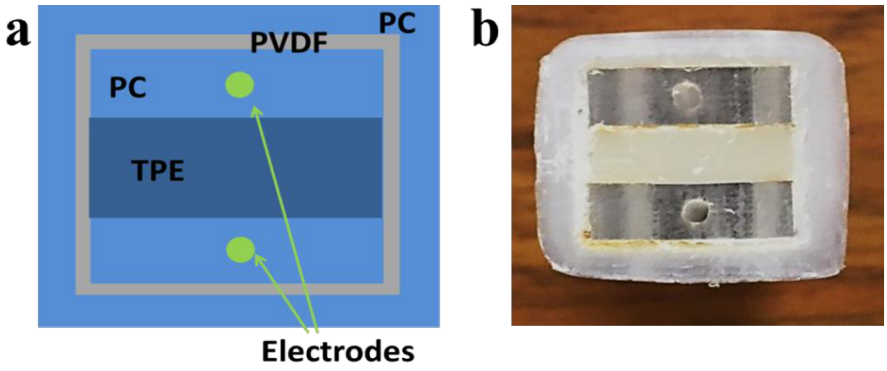

Figure 3-10 (a) Schematic of a PC/PVDF/TPE fiber structure (b) Cross section image of a preform before drawing

The final preform fabrication steps are as follows:

1. First the 1 mm TPE extruded films are stacked in an 18 mm-wide C-shape aluminum mold and are pressed in a vacuum oven at 190 ºC to form a solid center plate.

2. Four 18 mm-wide PC or PMMA are milled into thin plates and semicircular groove is milled on one side of the plates with a ball-end mill. The thickness of the plate and the groove can be around 2.5 mm and 1.5 mm.

3. The four plates are then placed on the top and bottom side of the TPE center plate, and the assembly is consolidated in the vacuum over again. The temperature is 135 ºC if using PMMA and 180 ºC if using PC. During this step, the semicircular grooves on each side form a complete circular channel for the copper electrodes.

4. The core perform is wrapped with a thin layer of PVDF or LDPE film, followed by PC or PMMA film. The size of the final preform is usually 25 mm.

5. The preform is pressed for the third time in the vacuum oven in a 25 mm C-shape aluminum mold. The preform is usually consolidated twice with a 90 ºC rotation to ensure all four sides are equally pressed. The first two consolidation processes can sometimes be combined when pairing PC with TPE since their processing temperature is close. **Figure 3-11** shows the workflow of the preform fabrication process.

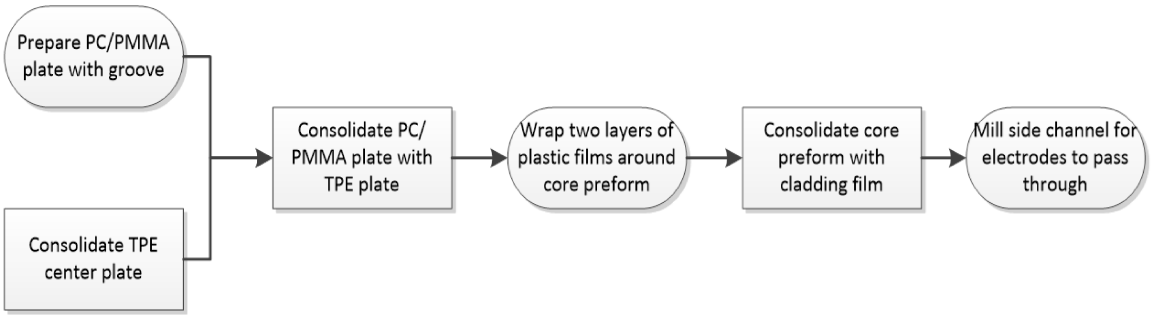

Figure 3-11 Flowchart of the preform fabrication steps

The size of the hollow channels in the top and bottom PC or PMMA plates is chosen to match the diameter of the copper electrodes multiply the draw-down-ratio from the preform to fiber. The two wires are passed through the channel before the drawing and are confined in the hard layers once the fiber is drawn to the final diameter. The drawing temperature is 150/285/120 ℃ for the PC/PVDF/TPE combination and 140/240/100 ℃ for the PMMA/LDPE/TPE combination. Images of the drawn fiber before and after DCM etching are shown in **Figure 3-12**. By adjusting the relative geometry of each layer in the preform and the draw-down ratio, the fiber can be drawn from 1 mm to 300 μm with 125 μm, 80 μm and 50 μm copper electrodes.

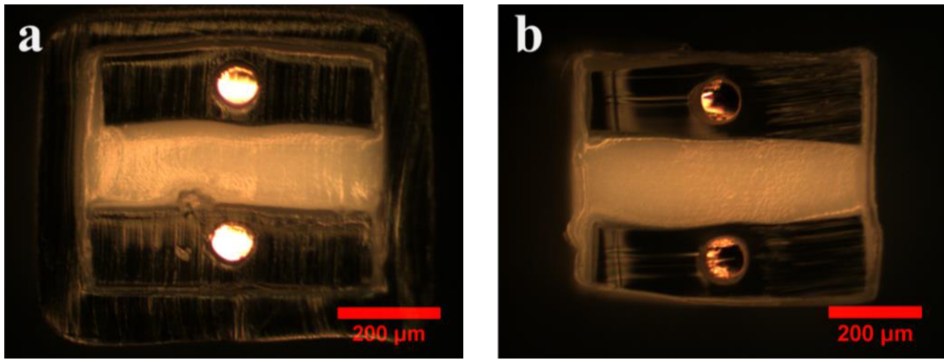

Figure 3-12 (a) Optical microscopic photo of the PC/TPE/PVDF fiber with 80 μm copper electrodes (b) Optical microscopic photo of the same fiber after cladding etched with DCM

When the copper wire diameter is 125 μm or 80 μm, passive feed scheme shown in **Figure 3-3** was used. The draw force pulls the copper wires from the spool which rotates around a ball bearing. However, when the electrode diameter is further reduced to 50 μm, occasional breakage can happen. The reason is that the reduced diameter leads to a smaller maximum force the

copper wire can sustain. To overcome the issue, we have tried to replace copper wires with tungsten wires since tungsten has a much higher tensile strength. The fiber with 50 μm tungsten wires was successfully fabricated with the same polymer/elastomer structure, and the fiber spool is shown in **Figure 3-13 (a)**. The downside of choosing tungsten is the reduced conductivity compared to copper. Electroplating a layer of copper is likely to solve the problem since most of the high-frequency current is distributed on the surface due to skin effect. The alternative is to use an active feeding system that the wire spool rotates to release wire with a speed matching the fiber capstan. A DC motor was later installed to the top of the draw tower as shown in **Figure 3-13 (b)**. By adjusting the voltage controlling the motor, the copper wires can experience a minimum pulling force from the fiber. Cross section images of PC/PVDF/TPE fibers with 50 μm copper wires are shown in **Figure 3-13 (c)** and **(d)**. The size of the etched fiber is 360 μm.

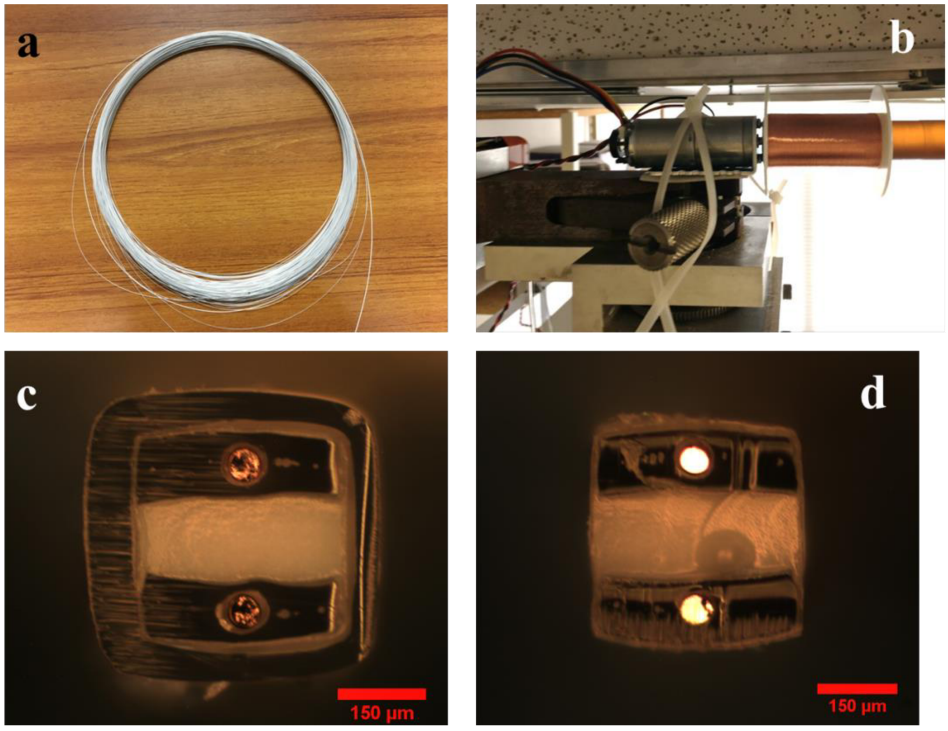

Figure 3-13 (a) 50 μm Tungsten electrode embedded polymer fiber, (b) DC motor with a 50 μm Tungsten spool mounted on the draw tower for active wire feeding (c) TPE fiber cross section before etch (d) TPE fiber cross section after etch

Chapter 4 Measurement and Result

4.1 Interrogation System Setup

As discussed in Chapter 2, two distributed sensing systems can be used to interrogate the electrode-embedded fibers: Time Domain Reflectometry (TDR) and Frequency Domain Reflectometry (FDR). Both methods have been explored in this project.

For the TDR method, a pulse generator (AFG3252, Tektronix) and a high-speed oscilloscope (Wavepro7Zi, LeCroy) were used to excite a pulse signal to the sensing fiber and to receive the reflection from the polymer fiber under test. The spatial resolution is determined by the pulse width and the speed of the oscilloscope. Compared to the 20 GHz-bandwidth oscilloscope, the 240 MHz signal generator limits the spatial resolution of the system. The minimum excitation pulse width was 5 ns, and the pulse would cover 1.2 m distance (if the velocity factor of the fiber is 0.8). The system setup and a typical waveform received at the oscilloscope end are shown in **Figure 4-1**. The fiber used here is the LDPE hollow fiber shown in **Figure 3-6 (c)**, and the fiber length is 5 meters. Three peaks representing the excitation pulse directly going into the oscilloscope, the reflection between the BNC coaxial cable and the fiber, and the end reflection of the fiber can be observed. The region between the two dashed green lines represents the fiber under test.

Qualitative tests with the hollow PE fibers were conducted using the same fiber placed on a flat surface with end reflection terminated and a weight of 360 gram was placed on a segment of 2.5 cm of the fiber. The weight was moved 5 cm for each subsequent measurement, and the reflection signals were recorded. The system schematic and the photo of the fiber under test are shown in **Figure 4-2 (a)** and **(b)**. The particular section of the reflection signal is also shown in **Figure 4-2 (c)** and a clear trend of time delay increase can be observed. The shift of the dip was calculated by correlation. There is a good linear relationship between the location of the weight and the time delay despite the current pulse width to be 5 ns. However, to increase the spatial resolution, FDR method was adopted for all the following experiments.

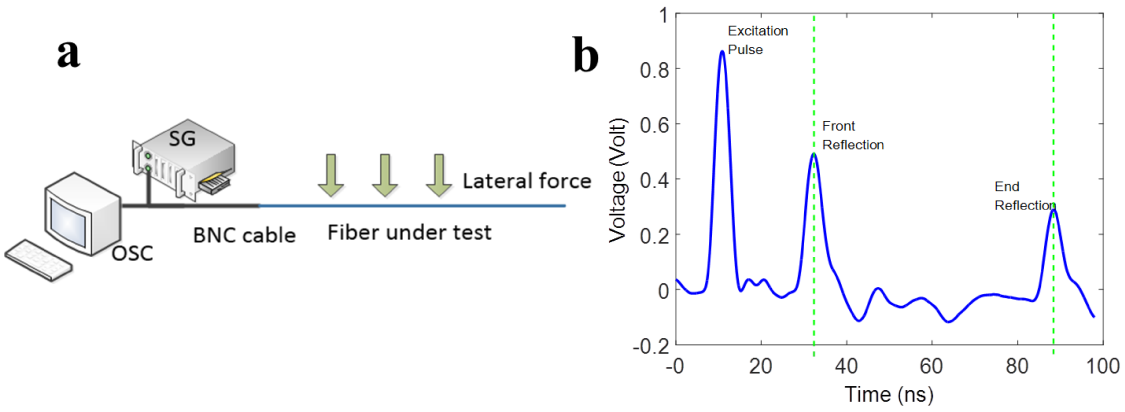

Figure 4-1 (a) Schematic of TDR interrogation system for pressure sensing fiber, (b) Time-domain reflection signal received by the oscilloscope

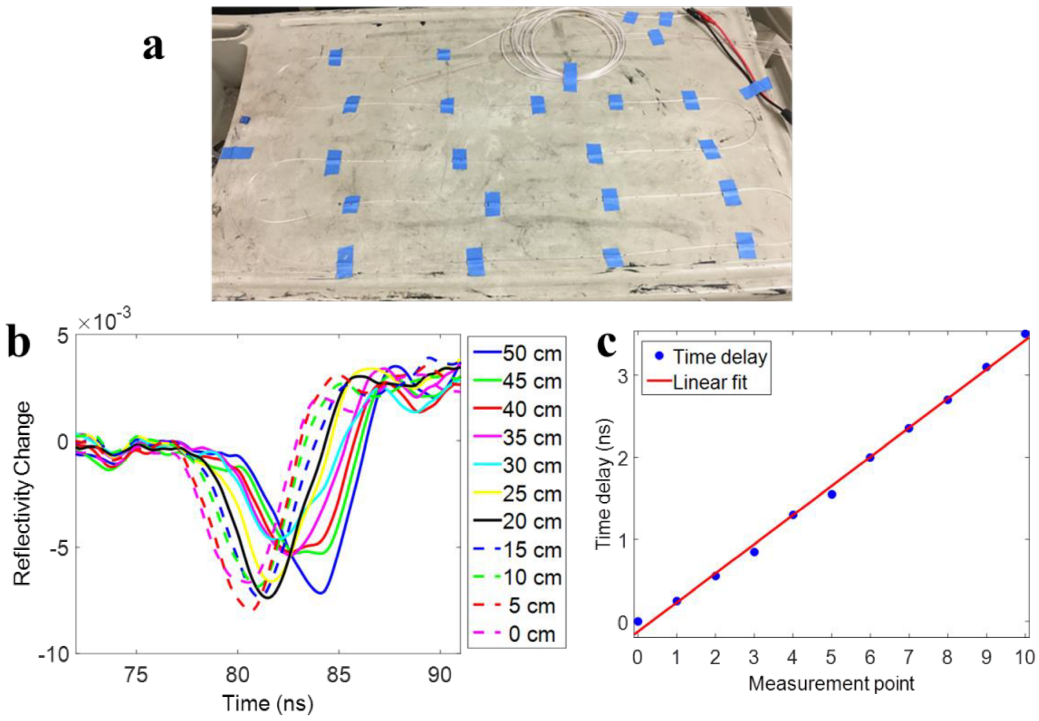

Figure 4-2 (a) 5 m of LDPE hollow fiber interrogated by the TDR system (b) Reflection coefficient change detected by the TDR system (c) The linear fit of the time delay vs. pressed location

A vector network analyzer (VNA 8753D, HP) for frequency scanning and analyzing the received results was used in the FDR system. The VNA was connected to the polymer fiber through an SMA coaxial cable, and the reflection parameter S11 was being monitored continuously. The

recorded results were an array of magnitude and phase values from each frequency step. The VNA performed inverse Fourier Transforms internally, and the frequency domain signal was transformed into time domain. **Figure 4-3** shows an example of the frequency signal and the transformed time-domain signal. One meter of the LDPE hollow fiber was connected to the VNA. The VNA scans the frequency from 3 MHz to 4803 MHz with a 3 MHz increment. The frequency responses shown in **Figure 4-3 (b)** and **Figure 4-3 (c)** are transformed into the time domain signal shown in **Figure 4-3 (d).**

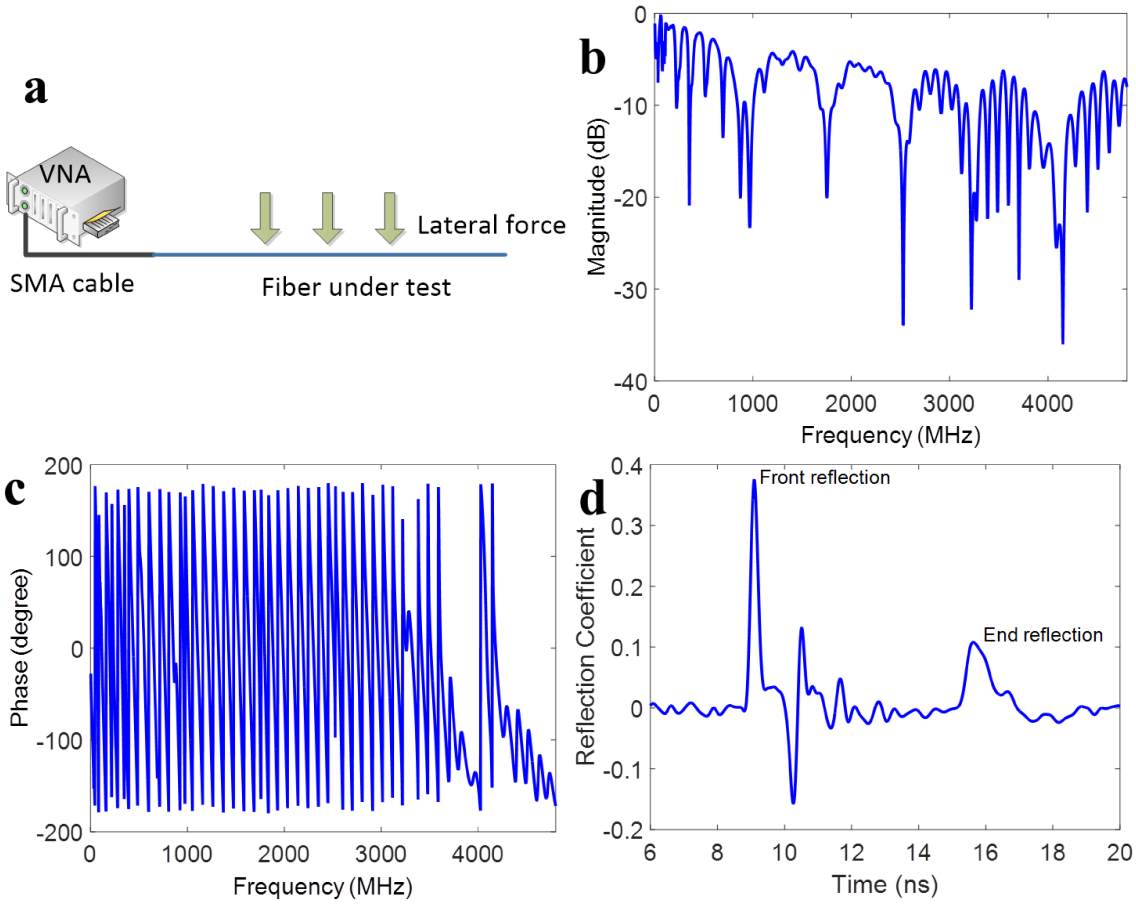

Figure 4-3 (a) Schematic of FDR interrogation system for pressure sensing fiber, (b) and (c) magnitude and phase data collected by VNA, (d) Time domain reflection coefficient information calculated from the frequency scan

In the FDR system, the measurement range and the spatial resolution is determined by the frequency scanning range and the step. The following formulae dictate the relationship:

$$Range = \left(\frac{1}{\Delta f}\right) \times VF \times c = \frac{N-1}{\Delta F} \times VF \times c$$

$$Response\ resolution\ \approx 1/\Delta F \tag{4-1}$$

Where Δf is the frequency step, VF is the velocity factor, c is the speed of light, N is the number of steps and ΔF is the difference between the minimum and maximum frequency. To maximize both the range and the spatial resolution, the number of the frequency steps was selected to be the highest available value 1601 and the frequency scanning range was set to be 4.8 GHz. The maximum detection range was calculated to be 80 m assuming the velocity factor to be 0.8, and due to the nature of reflection measurement, the actual range was 40 m. The calculated response resolution was 208 ps, which is equivalent 50 mm (VF = 0.8). For reflection measurements, because of the two-way travel time, the minimum resolvable separation is half of this value or 25 mm.

4.2 RF Transformer for Low-reflection Connection

Large front reflections can be seen in **Figure 4-1 (b)** and **Figure 4-3 (d)**, representing the impedance mismatch between the 50 Ω standard coaxial cable and the electrode-embedded fiber used in the measurement. As shown in Figure 2-1 (b), the parallel wire transmission line has an impedance greater than 100 Ω. The singular point reflects large portion of the excitation signal thus a solution to minimize the impedance mismatch is required. For majority of the fiber design used in this work, the impedance of the fiber is between 150 and 250 Ω, therefore a 1:4 RF transformer was used for impedance matching. The RF transformer follows the general principle: when signal current passes through the primary winding of the transformer, the current generates a magnetic field which couples to the secondary winding. When a load, such as a fiber in our case is connected to the secondary winding, an AC current will flow to the load. Based on the Faraday's law, the transformer follows the equations:

$$n = \frac{N_2}{N_1}, V_2 = nV_2$$

$$I_2 = \frac{I_1}{n}, Z_2 = n^2 Z_1 \tag{4-2}$$

The output voltage V_2 equals turn's ratio n times the input voltage V_1 while the output current I_2 equals the input current I_1 divided by turn's ratio n. The overall effect is that the output impedance Z_2 is input impedance Z_1 times the square of the turn's ratio. The turn's ratio of 1:2 would ensure the impedance at the secondary winding is 200 Ω, which is close to the fibers we are using. Since the VNA frequency scanning covers frequency from 3 MHz to 4803 MHz, a wideband RF transformer is needed. An RF transformer TCM4-452Z+ from Mini Circuit was selected, which has the required impedance ratio and a wide frequency range of 20-4500 MHz. The electrical schematic is shown in **Figure 4-4 (a)** and the complete circuit is shown in **Figure 4-4 (b)**. As indicated by the schematic, the 50 Ω input is connected to the primary port 2 and 3 while the 200 Ω output is connected to the secondary port 4 and 6. The suggested PCB mounting design given in the datasheet has an output impedance of 50 Ω and is not suitable for our need, thus the width of the copper trace width is calculated. The copper trace and the back copper ground surface constitute a microstrip, and a simple online tool is used for trace width calculation [80]. For 1 Oz copper, 1/16" FR-4 PCB board used in this case, the trace width is calculated to be 117 mils for the 50 Ω primary port and 26 mils (1 mil is a thousandth of an inch) for the two 100 Ω secondary ports. To quickly fabricate the PCB, the board was first sprayed with black paint, and the layout was drawn on the surface by a laser engraver (Boss Laser). The paint on the illuminated area was removed by the 1064 nm laser, and the exposed copper beneath the paint was subsequently etched away in a $FeCl_3$ solution. An SMA connector, a required 0.25 pF capacitor, the RF transformer, and the fiber were soldered on the final PCB board. The reflection signal of a PC/PVDF/TPE fiber is shown in **Figure 4-5**. Compared to the result shown in **Figure 4-3 (c)**, the front reflection is reduced from 0.4 to 0.15. The end reflection of the fiber was also minimized by connecting the fiber to a variable resistor.

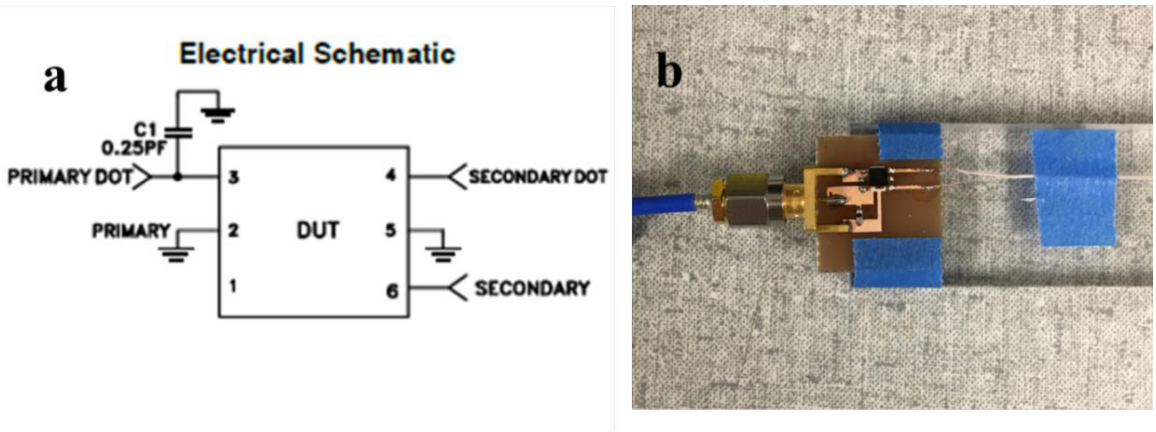

Figure 4-4 (a) RF transformer electrical schematic (copied from the data sheet) (b) RF transformer soldered to PCB, connecting SMA cable (left side) and fiber (right side)

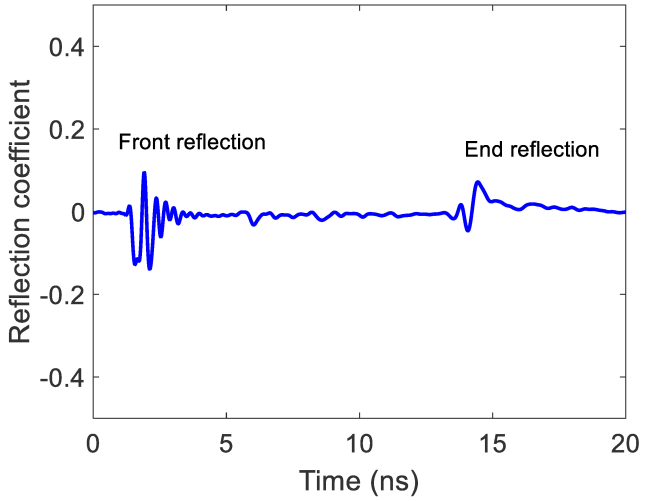

Figure 4-5 Reflection coefficient signal after inverse Fourier Transform of a fiber connected to the RF transformer

4.3 Result for Temperature Sensing Fiber

Temperature response of the fabricated PMMA fibers, LDPE fibers, and PVDF/PC fibers were evaluated by Frequency Domain Reflectometry with the VNA. To first demonstrate the temperature sensing capability, two sections of a 1.8 meter LDPE fiber with a pair of 125 μm diameter copper electrodes were attached to two thermoelectric coolers (TECs) shown in **Figure 4-6 (a)**. The TECs operate by the Peltier effect and are used to heat or cool the fiber attached on top. One end of the fiber was connected to the VNA with the RF transformer in between, and the

back reflection along the fiber was acquired. The scanning parameters remained the same: 3 MHz to 4803 MHz with 1601 steps. When both fibers were heated, two positive-negative peak pairs were observed. The positive peak corresponds to the temperature increase where the fiber is first attached to the TEC and the negative corresponds to fiber temperature resumes to room temperature. While keeping the second TEC unchanged, when the current passing the first TEC was revised, the TEC cooled the fiber on top, and the temperature change led to an inverse negative-positive peak pair. The result is shown in **Figure 4-6 (b)**.

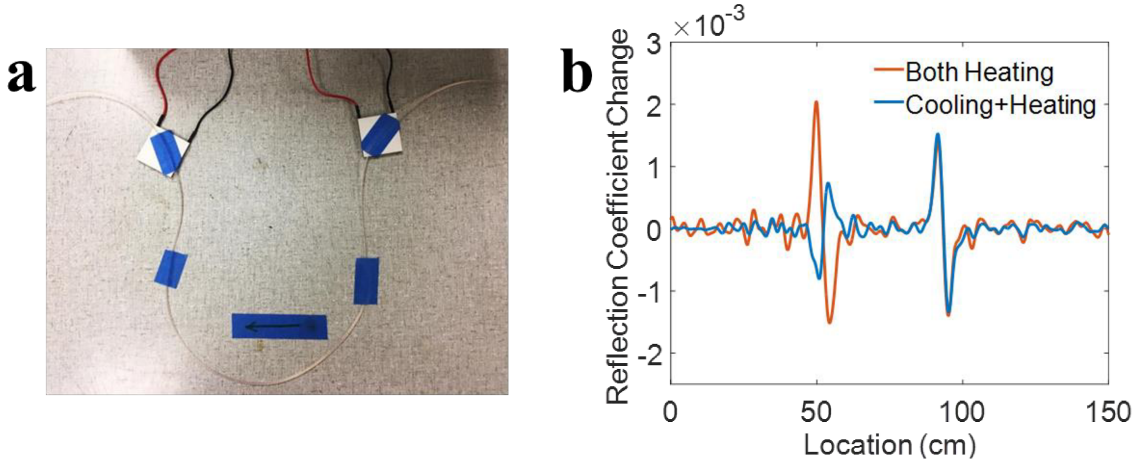

Figure 4-6 (a) LDPE fiber attached to two TECs, (b) Reflection coefficient change when the TECs are heated or cooled

To quantify the temperature response of the LDPE fiber, the fiber was passed through a small 5 cm-long electrical furnace. The temperature of the segment inside the furnace was heated from room temperature (23 °C) to 85 °C. A K-type thermocouple probe was also inserted to the furnace so the internal temperature can be determined. The system schematic and experiment setup are shown in **Figure 4-7 (a)** and **(b)**. At each temperature, the reflection coefficient signal was measured five times and the difference between the reference signals at room temperature was obtained (**Figure 4-7 (c)**). By tracking the positive peak height and plot against the temperature, a linear relationship between the temperature and the reflection coefficient change is revealed. The temperature response is calculated to be 9.8×10^{-5} $°C^{-1}$. The error bar shown in **Figure 4-7 (d)** is the standard deviation of the five measurements at each temperature.

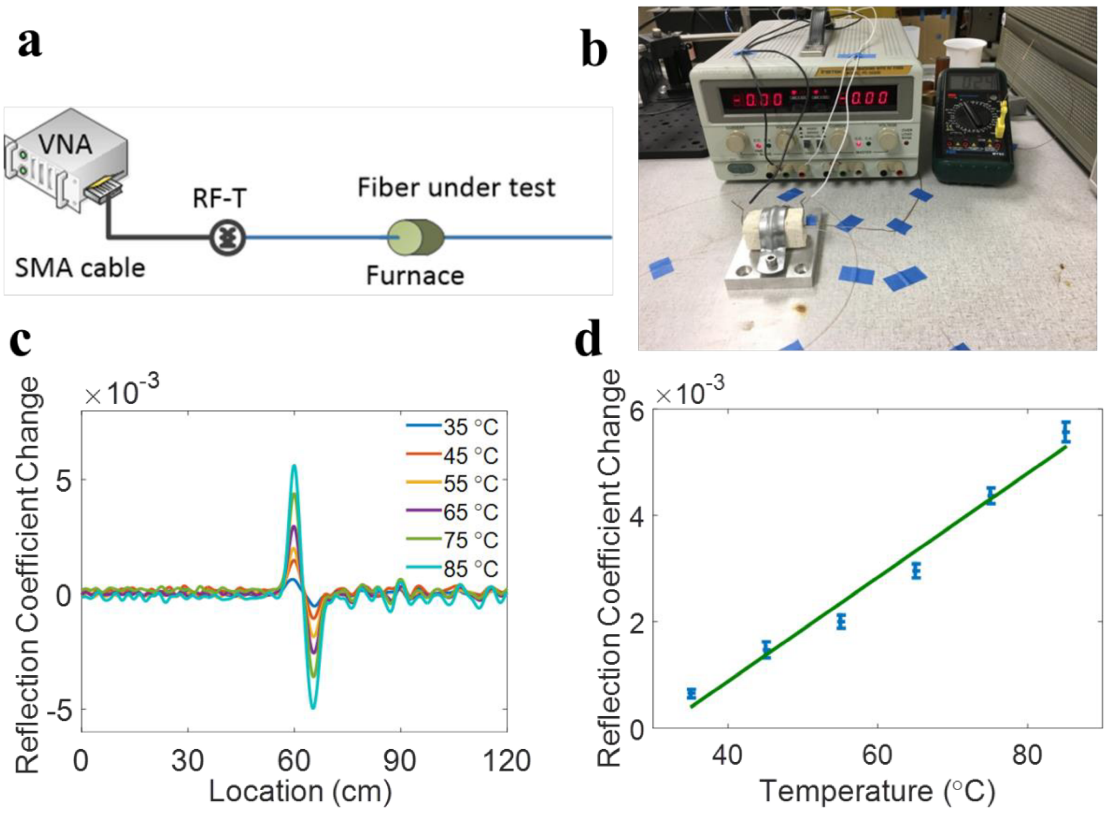

Figure 4-7 (a) Schematic of measuring temperature response of the LDPE fiber (b) system setup showing the fiber passing though the electric furnace. A current source for the furnace and a multimeter capable of reading temperature are shown in the back (c) reflection coefficient difference compared to the room temperature value (d) calibration curve for the LDPE fiber.

The temperature resolution of the system is dependent on the thermocouple accuracy, the resolution of the VNA and the random signal variation from the fiber. The VNA's resolution is much higher than the other two thus. On the one hand, the thermal couple reading on the multimeter has a minimum resolution of 1 °C on display, and we assume that its actual accuracy is higher. On the other hand, the maximum standard deviation from the measured result is 1.86×10^{-4} which corresponds to 2 °C based on the calculated sensitivity. Therefore we can make a very conservative estimation that the LDPE fiber can distinguish 2 °C temperature change. By recording the temperature with a higher accuracy thermocouple reader and increasing the data acquisition and average times, it is very likely that the temperature resolution of the system can be improved. The spatial resolution is limited by the frequency step and the furnace

size. The estimation in section 3.1 suggested the theoretical limit to be 25 mm, so the actual spatial resolution here is limited by the furnace size, which is 50 mm.

The PVDF/PC fiber with copper electrodes was measured under the same condition. For LDPE, its positive thermal expansion and negative temperature dependence of permittivity increase the LDPE fiber's local impedance together when it is being heated. PVDF has a positive temperature dependence of its permittivity [78], which would lower the local impedance of the fiber upon heating. The reported thermal expansion coefficient of PVDF is only $0.7\sim1.8\times10^{-4}$ [74] and the permittivity increase reported in [78] is very large and would have a dominant effect on the fiber impedance. Experiment results shown in **Figure 4-8** have confirmed the hypothesis. Unlike the positive-negative peak pair observed from the LDPE fiber, the response from the PC/PVDF fiber is negative-positive peak pair because the heated region has smaller impedance than the one at room temperature. At each temperature, the reflection was measured five times and the result with the error bar calculated from the standard deviation is shown in **Figure 4-8 (b)**. The sensitivity of 2.0×10^{-4} °C^{-1} is also twice as that for the LDPE fiber. However, the noise of the thermal response is also larger. The maximum standard deviation from the measured result is 5.38×10^{-4} which corresponds to 2.7 °C. Therefore, we can conclude that the two fibers have comparable performances.

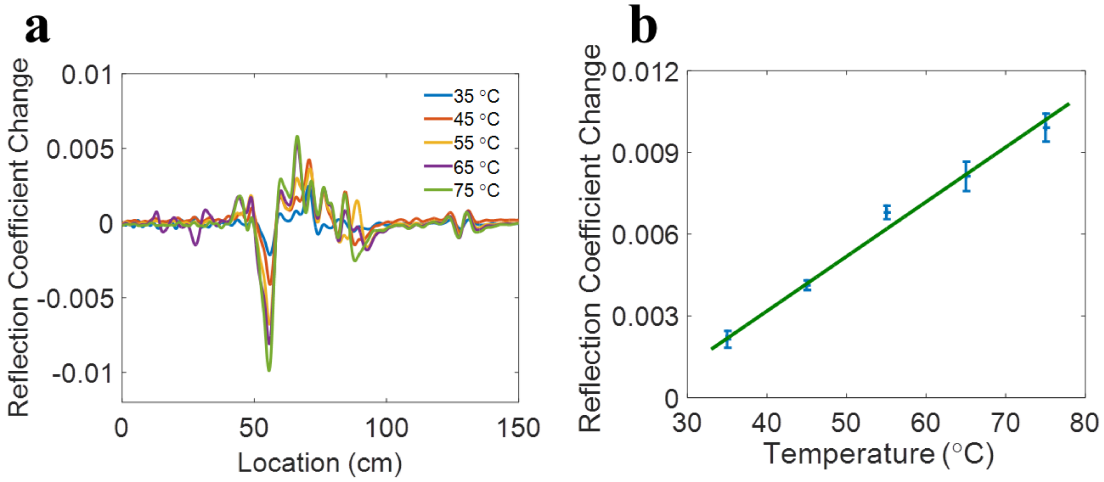

Figure 4-8 (a) Reflection coefficient difference compared to room temperatures, (b) calibration curve for the PVDF/PC fiber.

We have also tested the PMMA fiber with the embedded electrodes with the same system. Similar to PVDF, PMMA is reported to have a positive temperature dependence of its permittivity [76, 77]. However, when the fiber was heated in the furnace from room temperature to 95 ºC, no appreciable change was observed in the reflection signal, as shown in **Figure 4-9**. The most probable reason is that the effect of PMMA's thermal expansion and the increase of permittivity upon heating partially cancel each other out. The remaining effect is much weaker than the LDPE or PVDF case thus can't be detected with confidence in our system.

It is worth mentioning that the temperature response of the fiber is directly related to the polymer's intrinsic material properties, such as the thermal expansion coefficient and the temperature dependence of permittivity. Therefore, the sensitivity should be the same for a specific fiber at every point along its length. In reality, fiber transmission loss reduces the amplitude of the reflection peak, and the reduction increases with the distance. As a result of the signal intensity reduction, points on the fiber away from the VNA seem to have a lower sensitivity. This can be addressed by post-processing in Matlab and the discussion is in section 4.5.

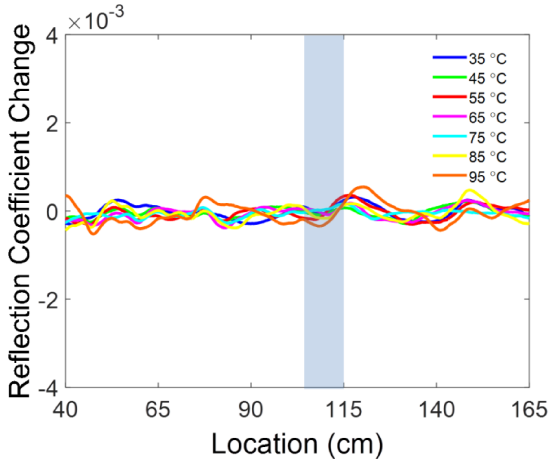

Figure 4-9 Reflection coefficient difference of PMMA fiber compared to room temperature, shadow region represent the heated section

4.4 Result for Pressure Sensing Fiber

For the LDPE hollow structure fiber and earlier iterations of the TPE fibers (fibers shown in **Figure 3-6** and **3-8**), we have fixed those fibers on the test table, and applied pressure on the fiber surface, moving 25 mm with each measurement. In both cases, the reconstructed pulse width matched well with the theoretical calculation and is much narrower than the pulse generated by the 240 MHz signal generator used in the TDR system. The clearly separated pulse array confirmed that the spatial resolution of 25 mm could be achieved by the FDR system. **Figure 4-10** shows the time-domain signal collected by the VNA. For the PMMA/TPE fiber, a negative-positive peak pair can be more clearly observed, which confirms that the impedance is smaller in the pressed area. Due to the unstable drawing of the two types of fibers, the measurements are mainly showing the fiber's capability of locating the pressure point.

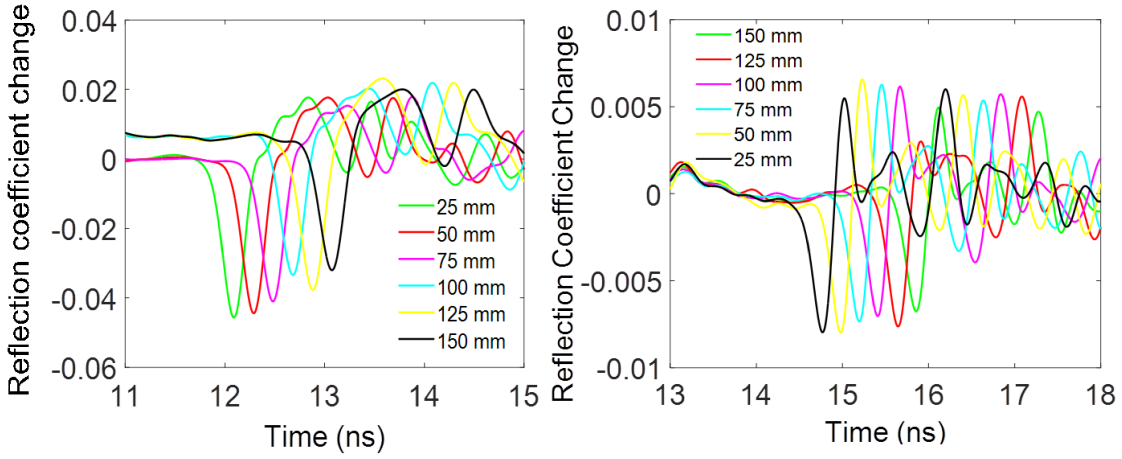

Figure 4-10 (a) Reflection signal for LDPE hollow fiber, (b) Reflection signal for PMMA/TPE layered fiber

For the etched PC/PVDF fiber shown in **Figure 3-12**, detailed measurements were conducted. The VNA performed the same frequency scan from 3 MHz to 4803 MHz for frequency domain reflectometry and the transformed time-domain result was compared with reference for each set of measurements. Pressure was first applied by hand to a 1.9 m fiber and each location being touched was 5 cm further downstream, starting from 80 cm of the fiber, as shown in **Figure 4-11 (a)**. The results in **Figure 4-11 (b)** show a series of negative-positive peak pairs corresponding to

the hand press. The equally spaced peak pairs confirm that location information can be extracted from the reflection on the time domain with this fiber. By tracking the time delay of the negative peaks, we were able to plot the time delay vs. location plot shown in **Figure 4-11 (c)**. A linear curve fitting based on Equation 2-4 helped us to determine the velocity factor to be 0.69.

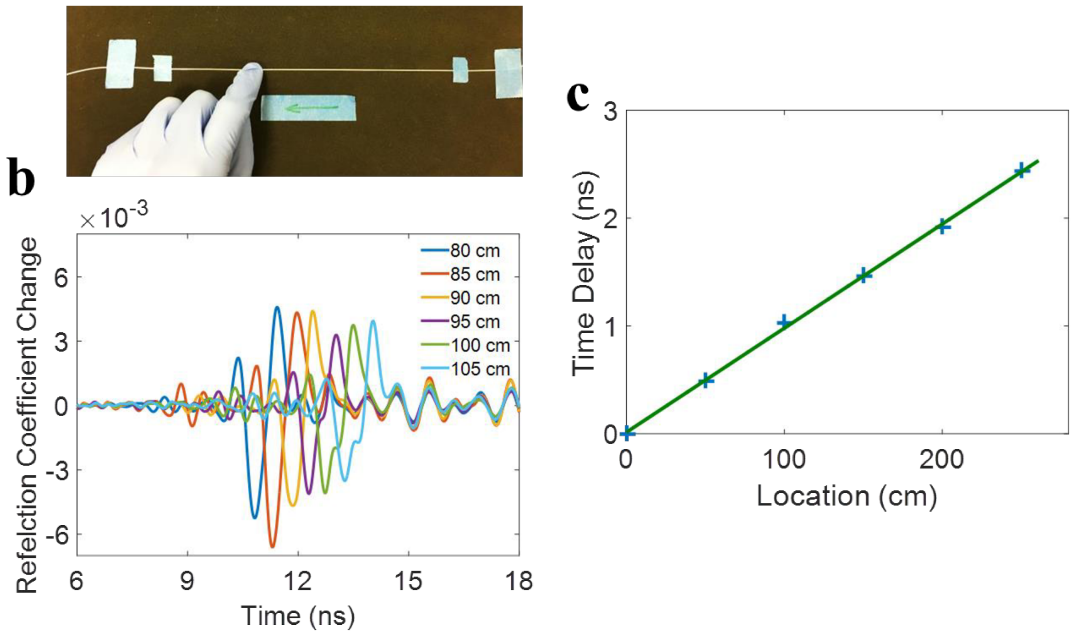

Figure 4-11 (a) Hand press the PC/PVDF/TPE fiber with 80 μm copper electrodes (b) reflection signal from the hand press (c) The time delay of the negative peak vs. the location of the press

To quantify the pressure response of the fiber, a Universal Testing Machine capable of applying precise pressure to a small surface area is preferred. In lieu of a commercial UTM instrument, a simplified test system was constructed with a linear stage and a digital scale to apply repeatable pressure to the fiber. The linear stage acted as an actuator to press the fiber when moved downward, and the scale was used as a force gauge to measure the pressure. As shown in **Figure 4-12 (a)**, the fiber was first fixed on a glass slide on top of the scale, and a plastic block was attached to the bottom of the linear stage. As the linear stage moved down, the block would touch the fiber under it and would further compress the fiber. The compression force was shown on the scale in grams. By dividing the contact area, we can calculate the actual pressure that was added to the fiber. Different weight between 10 g to 90 g was applied to the fiber at two locations, and the reflection was measured at each weight five times. The range of the pressure applied was between 10 kPa and 60 kPa, and the result is shown in **Figure 4-12 (b)**. The error

bar shown on the figure comes from the standard deviation of the five measurements at each point.

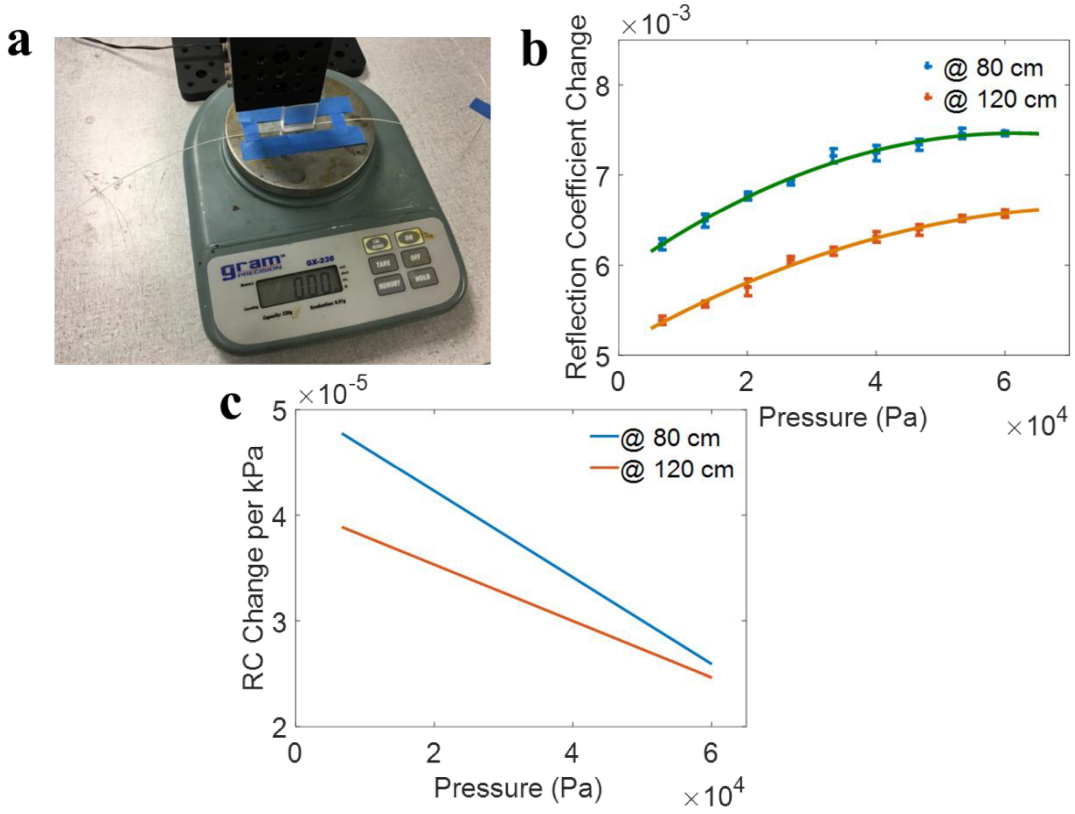

Figure 4-12 (a) Photo showing fiber is placed between the scale and a linear stage (b) pressure response of fiber at two locations (c) sensitivity of fiber vs. pressure at two locations

Unlike the temperature response discussed in the previous section, the fiber under test has a non-linear pressure response. The initial coefficient change is likely coming from the contact of between the polymer block and the fiber, and the lower change at 120 cm compared to 80 cm represent the transmission loss of the fiber. The pressure response shown in **Figure 4-12 (b)** can be fitted with 2nd order polynomials and the results are given here:

$$At\ 80\ cm: \quad \Delta\rho = -4.10 \times 10^{-7}p^2 + 5.05 \times 10^{-5}p + 5.91 \times 10^{-3}$$

$$At\ 120\ cm: \quad \Delta\rho = -2.67 \times 10^{-7}p^2 + 4.07 \times 10^{-5}p + 5.10 \times 10^{-3} \qquad (4\text{-}3)$$

Where $\Delta\rho$ is the reflectivity change and p is the pressure in kPa. The non-linear relation is expected, as the TPE would not have a linear pressure-compression curve. The pressure sensitivity can be calculated from Equation 4-3 and it decreases as pressure increases **(Figure 4-13 (c)).** At 60 kPa, the response is minimum (2.5×10^{-5} per kPa). If assuming a reflection coefficient of 10^{-4} can be differentiated, we can make a very conservative estimate that the pressure resolution is at least 4 kPa. Increasing the averaging time and the interrogation system can further increase the resolution.

We have also demonstrated the potential of incorporating the fiber into a grid structure. A continuous pressure-sensing fiber and segments of non-functional fibers were braided into a 15 cm by 20 cm grid, and the spacing between the pressure-sensing fibers is 2.5 cm, as shown in **Figure 4-13 (a)**. The VNA was connected to the sensing fiber from the lower end. Two 20 g blocks were placed on the grid and reflection signals corresponding to different scenarios were recorded by the VNA. In **Figure 4-13 (b)**, we show that one weight first created a peak pair at the 80 cm position. When the second weight was placed downstream at 105 cm, a new peak pair appeared while the initial feature remained the same. Lastly, when the pressure at the first location was increased by adding more weight (not shown in **Figure 4-13 (a)**), the amplitude of the reflection increased at the corresponding peak pair. Unfortunately, for the current grid, since the grid surface is no longer flat from the weaving, the pressure applied by the weight would not be uniform on the fiber. A denser weaving with more non-functional fibers is expected to distribute pressure more evenly to the sensing fiber.

Finally, we evaluated the effect of transmission loss of the fiber. A constant load of 20 gram was applied to a longer fiber at different locations with one-meter separation, and the reflection spectra were shown in **Figure 4-14**. The peak height was reduced while the width was increased, due to the frequency dependent loss of the transmission line. The post-processing calibration is discussed in the next section.

We want to point out that since both temperature and pressure sensing fibers are based on a parallel wire transmission line structure, bringing a conductor to the close proximity of the fibers will generate a false reflection. This is because the conductor will interact with the

electromagnetic field of the transmission line, and the coupling alters the local characteristic impedance.

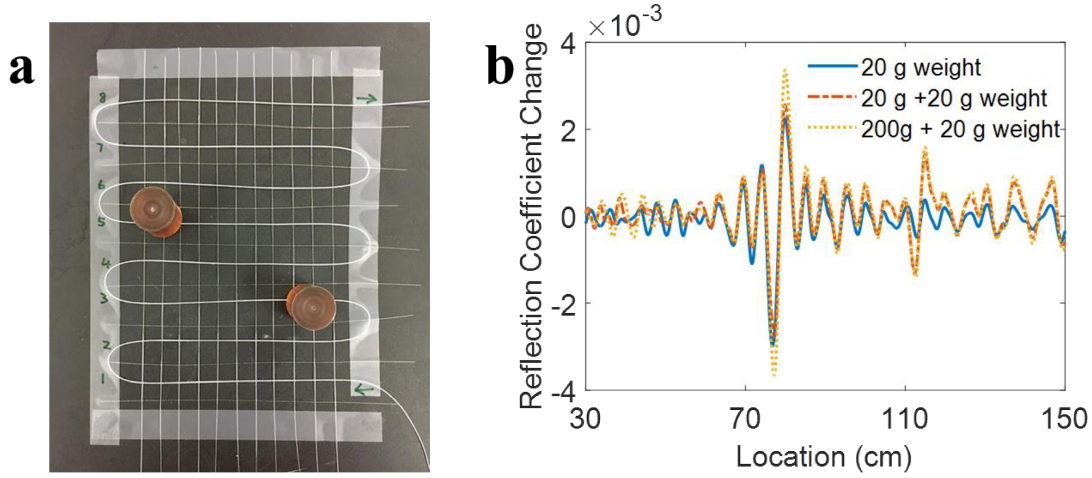

Figure 4-13 (a) A loose grid made by weaving a continuous pressure sensing fiber with non-functional short fibers (b) Reflection signal recorded by VNA in three scenarios

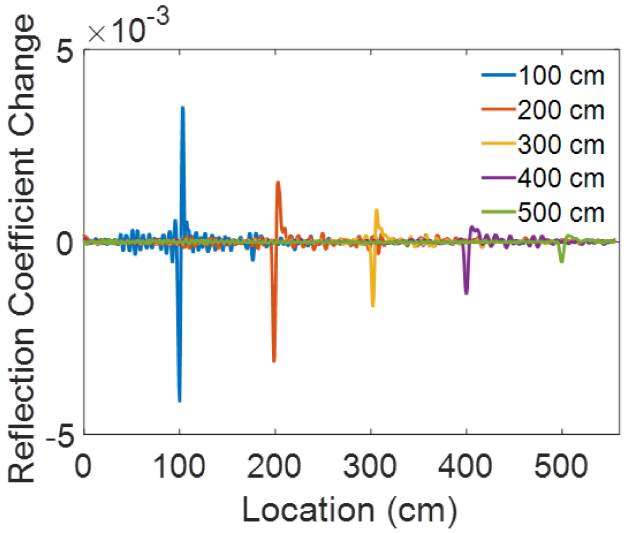

Figure 4-14 Pressure response of PC/TPE fiber at different point

4.5 Discussion

In this section, we discuss three relevant topics with the electrode-embedded fiber, including the transmission loss, the long-term stability, and further attempts to improve the pressure sensitive fiber structure.

4.5.1 Fiber Transmission Loss

As shown in **Figure 4-14**, the peak height of a PC/PVDF/TPE fiber's pressure response drops as the distance increases. This is due to the intrinsic transmission line loss described below [58]. Besides the impedance given in Equation 2-2, the propagation constant is another important parameter of a transmitssion line, given in Equation 4-4 here.

$$Y = \sqrt{(R + j\omega L)(G + j\omega C)} \tag{4-4}$$

The attenuation is the real part of the propagation constant:

$$\alpha = real(Y) \approx \frac{R}{2} \cdot \sqrt{\frac{C}{L}} + \frac{G}{2} \cdot \sqrt{\frac{L}{C}} \approx \frac{R}{2Z_0} \approx \sqrt{\frac{f\pi\epsilon}{\sigma_c}} \cdot 1/[d \cdot \operatorname{acosh}\left(\frac{D}{d}\right)] \tag{4-5}$$

Where f is the frequency, ε is the permittivity of the dielectric material, σ_c is the conductivity of the metal material, and D and d are the distance between the electrodes and the diameter of the electrode. The formula indicates that frequency, electrode diameter, and distance between the electrodes all affect the attenuation. For a 1 GHz sine wave, 125 μm diameter wires with a distance of 600 um, relative permittivity of 2, copper's conductivity being 5.96×10^7 S/m, the attenuation is 0.11 Np/m thus the signal will experience a 19 dB loss over 20 meters of fiber. If the attenuation is frequency-independent, it is easy to compensate the transmission loss from the time-domain reflection signal acquired from the VNA. The frequency dependent transmission loss not only reduces the amplitude of the reflection but also broadens the signal. A post-processing scheme is proposed and is demonstrated in Matlab.

Consider three reflection points of impedance mismatch located on a lossless transmission line at 0.7 m, 3 m, and 7 m. The amplitude of the reflection is 0.01 in all three cases. The EM wave speed is simplified to the speed of light in vacuum (assuming the velocity factor is one for simplicity). When a VNA performs a frequency scan, at each frequency step, from Equation 2-5 and 2-6, we know the return signal is the superposition of the Fourier transform of the three reflections, shown in **Figure 4-15 (a)** and **(b)**. Here we use the same frequency scanning parameters: 3MHz to 4803 MHz with 1601 scanning point. It can be observed that the amplitude of the frequency response from each reflection points is the same, and the difference is that the oscillation is faster for points further downstream. The reconstructed time-domain (or space-

domain) signal shown in **Figure 4-15 (c)** was calculated from the simulated FFT spectrum after applying a Hann window. Although the window function reduces the reflection peak height to half, the three peaks can be resolved with comparable amplitude.

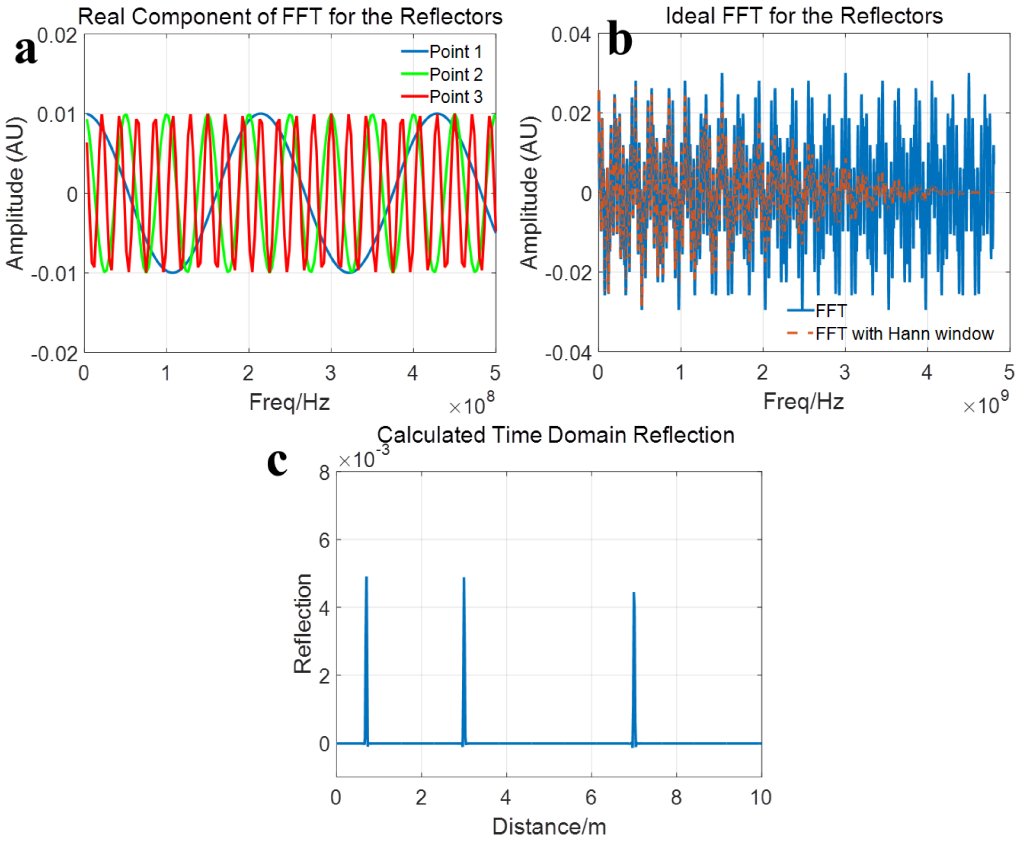

Figure 4-15 (a) Real component of the frequency responses of the three reflectors, only showing 3~500 MHz for better viewing (b) total frequency response from the three reflectors and the result after multiplying a Hann window (c) reconstructed reflection signature from inverse Fourier Transform.

When the transmission line has a frequency-independent loss, the frequency scanning signal is attenuated by a position-dependent factor $AF_i = \exp(-2z_i \cdot \alpha)$. Therefore the amplitude of the frequency response is different for each reflection point, shown in **Figure 4-16 (a)**. The resolved time-domain reflection from the distorted frequency response shown in **Figure 4-16 (b)** renders smaller peak height for the points further downstream. Because the attention is frequency independent, even though the frequency response was distorted, the calibration can be readily performed in the time-domain by multiply an inverse factor $AF_i^{-1} = \exp(2z_i \cdot \alpha)$. The distorted

and calibrated data is also given in Equation 4-6 to 4-8 (the relative permittivity is assumed to be unity). The calibrated result shown in **Figure 4-16 (c)** is identical to the lossless scenario shown in **Figure 4-15 (c)**.

$$H(\omega) = \sum_{i=1}^{N} AF_i \cdot \Gamma_i \cdot \exp[j(^{-2z_i\omega}/_{c})] \tag{4-6}$$

$$h(t) = \sum_{i=1}^{N} AF_i \cdot \Gamma_i \cdot sinc[(\omega_{max} - \omega_{min})(t - \tau_i)] \tag{4-7}$$

$$h'^{(t)} = \sum_{i=1}^{N} AF_i^{-1} \cdot AF_i \cdot \Gamma_i \cdot sinc[(\omega_{max} - \omega_{min})(t - \tau_i)] \tag{4-8}$$

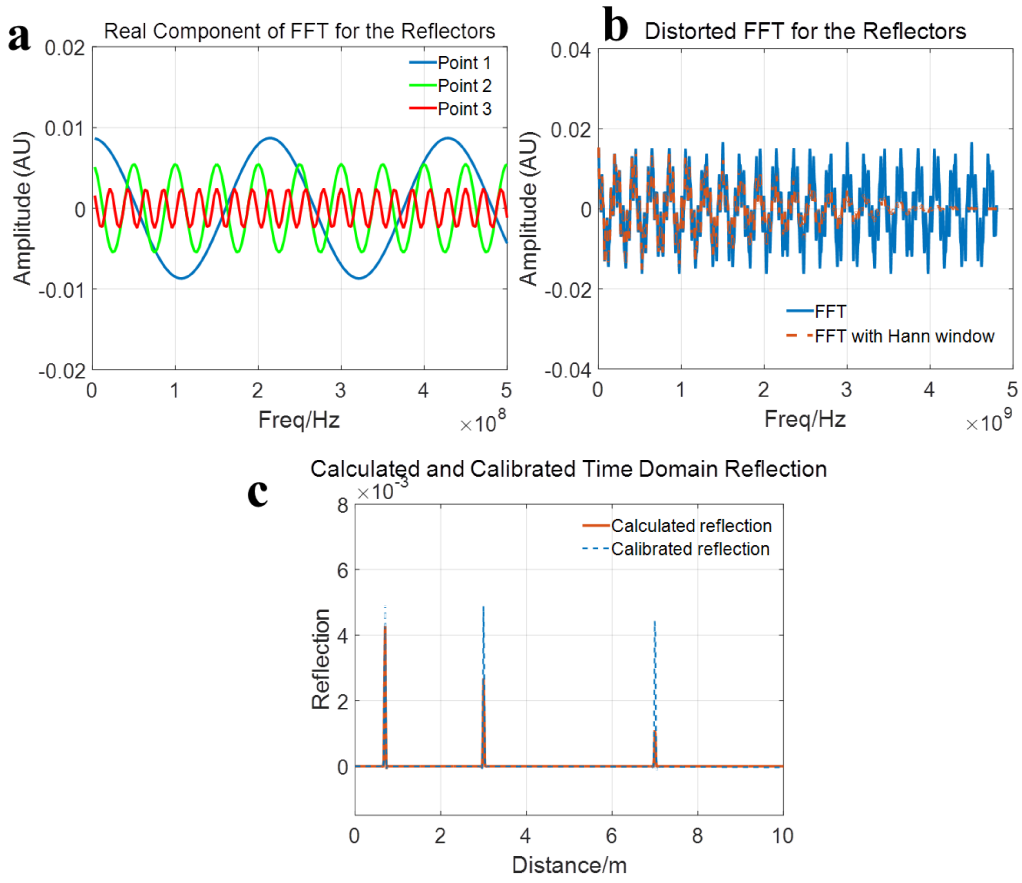

Figure 4-16 (a) Real component of the frequency responses of the three reflectors, the transmission line has a 0.1 Np/m attenuation coefficient, only showing 3~500 MHz for better viewing (b) total frequency response from the three reflectors and the result after multiplying a Hann window (c) reconstructed reflection signature from inverse Fourier Transform and the calibrated reflection result.

In the real situation, the attenuation coefficient is proportional to the square root of frequency. Therefore the amplitude of the frequency response of each reflection point decreases with frequency, and the decrease rate is position-dependent, as shown in **Figure 4-17 (a)**. The supposition of the three yields a more distorted total frequency response shown in **Figure 4-17 (b)** and the resolved time-domain reflection is given in **Figure 4-17 (d)**. It can be seen that the peaks from the orange curve are lower and wider, which is in accordance with the experiment result shown in **Figure 4-14**. This is because the multiplication in the frequency domain of the original frequency response and the attention factor $AF_i' = \exp(-2z_i \cdot \alpha_f) = \exp(-2z_i \cdot B\sqrt{2\pi\omega})$ becomes convolution of the two in the time domain. The overall time-domain signal is the summation of each convolution, so it is difficult to separate each sum term and run deconvolution. In order to resolve the true signal, the distorted time-domain result is treated as an estimation of the genuine signal, and each point is transformed back to the frequency domain separately where the position-dependent correction term $AF_i'^{-1} = \exp(2z_i \cdot \alpha_f) = \exp(2z_i \cdot B\sqrt{2\pi\omega})$ is applied. After summation of corrected Fourier transform from each point, the calibrated frequency response is acquired (**Figure 4-17 (c)**) and a second inverse transformation gives the calibrated time-domain signal, shown in **Figure 4-17 (d)**. Equation 4-9 to 4-12 describes the calibration process. By comparing the two blue traces in **Figure 4-15 (c)** and **Figure 4-16 (d)**, we can conclude that the method is effective. However, due to the exponential multiplication used for generating the calibrated frequency response, the high-frequency component shown in **Figure 4-17 (c)** becomes very large. This would inevitably introduce noise in the temperature-domain signal. In the real case, the effectiveness of this method is also affected by the signal to noise ratio of the system.

$$H(\omega) = \sum_{i=1}^{N} AF_i' \cdot \Gamma_i \cdot \exp\left[j\left(-2z_i\omega/c\right)\right] \quad (4\text{-}9)$$

$$h(t) = \sum_{i=1}^{N}\{\mathcal{F}^{-1}(AF_i') * \Gamma_i \cdot sinc[(\omega_{max} - \omega_{min})(t - \tau_i)]\} \quad (4\text{-}10)$$

$$H'(\omega) = \sum_{i=1}^{N}[\, AF_i'^{-1} \cdot \mathcal{F}(h_i(t)] \quad (4\text{-}11)$$

$$h'(t) = \mathcal{F}^{-1}[H'(\omega)] \quad (4\text{-}12)$$

In the equation, $B = \sqrt{\frac{\epsilon}{2\sigma_c}} \cdot 1/[d \cdot \text{acosh}\left(\frac{D}{d}\right)]$, $\mathcal{F}$ denotes the Fourier transform and $\mathcal{F}^{-1}$ denotes the inverse Fourier transform.

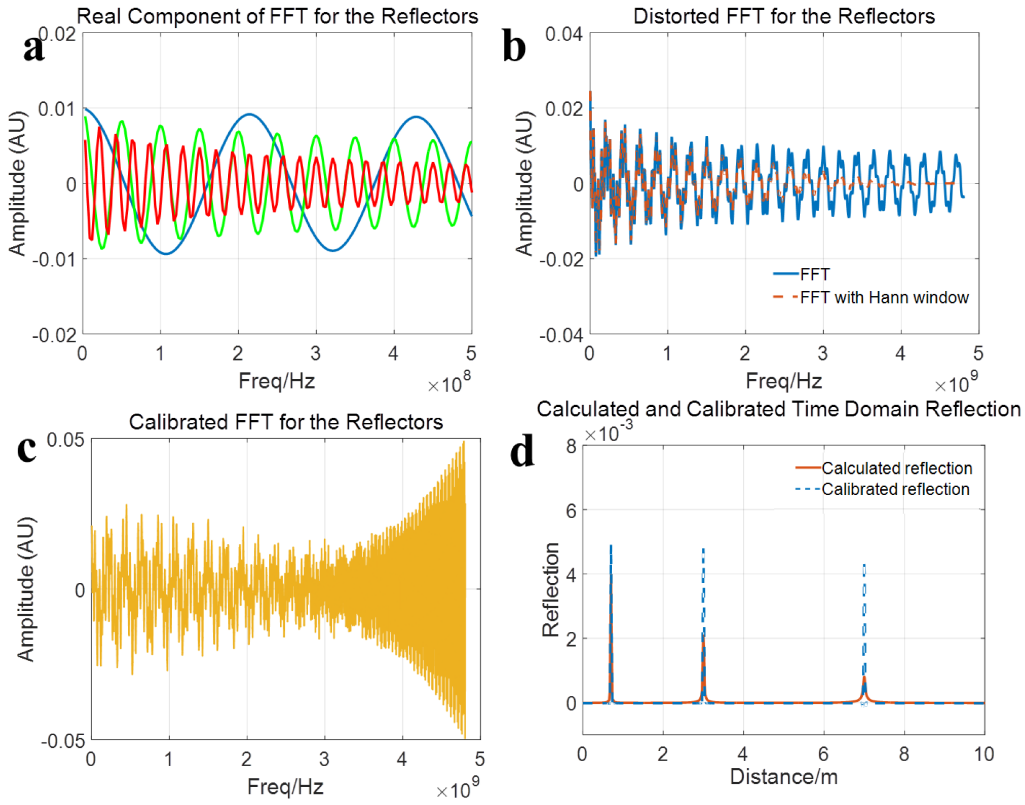

Figure 4-17 (a) Real component of the frequency responses of the three reflectors, the transmission line has maximum 0.3 Np/m attenuation coefficient at 4803 MHz, only showing 3~500 MHz for better viewing (b) total frequency response from the three reflectors and the result after multiplying a Hann window (c) calibrated frequency response (d) reconstructed reflection signature from direct inverse Fourier Transform and the calibrated reflection result from the calibration frequency response.

The proposed method is applied to the measurement result shown in **Figure 4-14**. The peak height at each location decreases because of the frequency dependent loss. From the fiber geometry, we know that the distance between the two electrodes is 350 μm, and the electrode diameter is 80 μm. The permittivity is calculated to be $\epsilon = \frac{\epsilon_0}{VF^2} = 1.86 \times 10^{-11}$, and the copper conductivity is 5.96×10^7. Therefore the attenuation coefficient is $\alpha = \frac{\sqrt{\frac{f\pi\epsilon}{\sigma_c}}}{\left[d\cdot\text{acosh}\left(\frac{D}{f}\right)\right]} = 5.82 \times 10^{-6}\sqrt{f}$. Since each trace shown in Figure 4-14 is the difference between the reflection signal

with and without the pressure, we apply the calibration method to the two signals and take the difference again. The new pressure response is shown in **Figure 4-18**. After the post-processing correction, the negative peak heights of each peak are more uniform, except for the last peak, which proves that the method is effective.

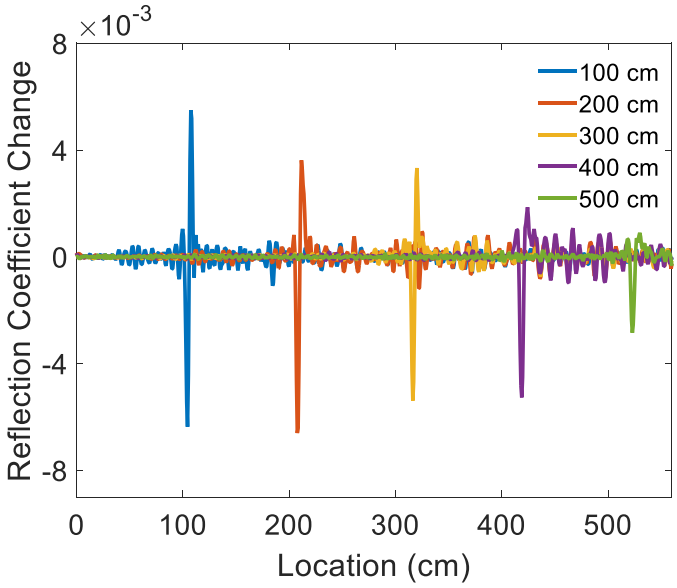

Figure 4-18 Corrected pressure response at different point

4.5.2 Long-term Stability

For temperature sensing fibers, the impedance change comes from thermal expansion or permittivity change of the polymer materials. Both changes are reversible and the fiber temperature response should be repeatable even after thousands of thermal cycles. The upper limit of the temperature range should be kept below the melting temperature of LDPE and PVDF so minimum softening will occur.

For pressure sensing fibers, the impedance change is related to the distance between the electrodes. When the TPE layer is under compression stress, permanent deformation (creep) can lead to signal drift. Creep can be measured by applying a constant stress and record the deformation overtime. For TPEs, compression set value is used to quantify the extent of compression deformation. Following the ASTM test method (ASTM D395), a TPE is

compressed to 25% deformation for a period of time and then given 30 min to recover. The final thickness is measured and the compression set value is determined by the following formula:

$$CB = [(t_0 - t_i)/(t_0 - t_n)] \times 100 \quad (4\text{-}13)$$

Where t_0 is the original thickness, t_i is the final thickness, and t_n is the thickness under compression. The compression set for CL2242 and CL2250 at 23 ºC after 22 h is 23 % and 20%. The 20% value means that when CL2250 is compressed to 75% of the original thickness and kept in room temperature for 22 h, the TPE will return to 95% of the original thickness. The 5% unrecovered thickness would be the source of signal drift. However, in the real case, the error would be much smaller. If we use the tensile stress value 1.52 MPa as approximation of the Young's modulus, 60 kPa compression pressure will only generate a 4% deformation (the actual deformation is even smaller because the compression v.s. deformation is not linear). The limited deformation should only lead to a small creep over time at low temperature. Characterization of actual creep curve of the TPEs is not included in this work.

4.5.3 New TPE Materials

During the course of this project, we have come across the work published by Qu et al. [41] on thermal drawing stretchable fibers with TPE materials. The three materials used are G1657 and G1652 from Kraton Performance Polymers and Wacker Geniomer 140. They have reported direct drawing of the three TPEs without any supporting thermoplastic polymer, such as PC or PMMA used in this work. We have tried to take advantage of the new materials and ordered G1657 and G1652 from Kraton's distributor. The Wacker Geniomer 140 was discontinued thus the vendor provided us a similar product Wacker SLM TPSE 345. Kraton G1657 and Wacker SLM TPSE 345 come in the form of small pellets while G1652 are in white powder form. In order to press the pellets and powers into a solid piece, a Teflon mold was made. The TPEs were placed in the mold and hot pressed under vacuum. **Figure 4-18** shows the mold, the G1657 pellets and a small Wacker polymer cut from a molded piece. All three polymers have been molded into 1 inch by 6 inch plates with a thickness ranging from 0.5 to 1 inch. The solid TPE preforms were subsequently drawn at the temperature reported in the reference. However, we

were not able to draw the fiber stably. The most probable reason is the low press pressure limited by our current set up. We have used Aluminum block on top of the pellets inside the Teflon mold to provide the compression force but the maximum pressure applied is around 1.5 kPa. The pressure values used in the reference work are 10 kPa for the two Kraton polymers and 100 kPa for the Wacker Polymer. Although we have increased the vacuum oven temperature during the molding and the pellets can indeed be pressed into a solid piece, we suspect that the mechanical strength of the TPE plate is much weaker. A commercial hot press can very likely mitigate this issue. By adding a thermoplastic PMMA cladding layer, we have been able to draw a PMMA/G1657 preform similar to the design reported in previous sections.

Figure 4-19 Mold for TPE pellets (top), molded TPE (left) and TPE pellets (right)

Chapter 5 Polymer Optical Fiber Raman Temperature Sensing

Another part of the project is to explore new optical sensing method with polymer optical fibers. The polymer fibers discussed in chapter 2-4 has no optical wave guiding capability, and the pressure and temperature detection are realized by electrical reflectometry. The result reported in this chapter is focused on Raman scattering based optical distributed temperature measurement system with polymer optical fibers. Raman scattering based system has been used in silica optical fibers and sapphire fibers [81, 82], but hasn't been reported with polymer optical fibers. Due to the large transmission loss from the fibers drawn in the lab, we have used commercial PMMA multimode fibers to demonstrate the feasibility.

5.1 Brief Discussion about Polymer Optical Fiber

There have been abundant books and research articles on polymer optical fibers [83-85]. Here we give a brief overview of polymer optical fibers. A simple waveguide such as a glass optical fiber or polymer optical fiber usually has two concentric layers called the core and the cladding. The refractive index of the core region is slightly higher than the cladding to promote total internal reflection, and the majority of the light is confined in the core region. By the number of guided modes in the core, optical fibers can be divided into single mode fibers and multimode fibers. Majority of the single mode fiber has a constant refractive index, but multimode fiber can have a constant index core or a graded index core. The latter was developed to reduce modal dispersion and increase data transmission bandwidth. The glass optical fiber picked up pace after the 1960s and has been the backbone of high-speed telecommunication system [86]. Currently, the best single mode fiber has an optical loss of less than 0.15 dB/km at 1550 nm. It has also been widely used to develop fiber optical sensor for various applications. The idea of using transparent polymer materials as an optical transmission media has long existed, but the most significant hurdle is the large optical loss intrinsic to the polymer materials. Polishuk [87] has reviewed the history and improvement of polymer optical fibers, and the result is presented here to provide the general information to the reader. The initial loss of PMMA based polymer fibers

is 1000 dB/km before Mitsubishi Rayon was able to reduce the loss to the theoretical material limit of 150 dB/km. While researchers continue to improve the bandwidth of the PMMA based polymer fiber, Prof. Koike and his colleagues have developed perfluorinated polymer fibers with a low transmission loss of 50 dB/km. Today, PMMA and perfluorinated polymers are still the major materials used in polymer optical fibers. Despite the attenuation, polymer optical fiber is widely used in commercial products due to its flexibility, light weight, and ease of use and handling. Three important application areas are industrial control, automotive and high-speed data transmission for Fiber-To-The-Home (FTTH) or Local Area Networks (LAN). Extrusion and thermal drawing are two common fabrication techniques, and microstructured polymer optical fiber was first developed in 2001 [88].

Other than the aforementioned usage in communication and illumination, a vast number of polymer optical fiber-based sensors have been reported [16-18, 89]. Among them, backscattering-based sensors have utilized Rayleigh scattering [17, 18, 90-92] and Brillouin scattering [16, 93] for distributed temperature, pressure and strain measurement. So far we have not seen Raman scattering based temperature sensing system with polymer optical fibers. Therefore, we wanted to explore the possibility and have demonstrated temperature measurement in the lab.

5.2 Raman Scattering Based Temperature Sensing

When light is transmitted in the fiber, except for being transmitted or the absorbed, inelastic scattering including Brillouin scattering and Raman scattering occurs along with the elastic Rayleigh scattering. Raman scattering is associated with the molecular vibration of the molecules. The longer wavelength component is the Stokes signal, and the shorter wavelength component is the Anti-Stokes signal. Their relative intensity is temperature dependent, and by measuring that, the local temperature can be resolved. **Figure 5-1** shows the principle of the distributed temperature measurement by relative intensity change of the Raman scattering signals. The intensity of Anti-Stokes signal is usually lower, but it increases faster than the Stokes signal. The temperature dependence for the ratio of the two is given in Equation 5-1 [94].

$$R(T) = (\frac{\lambda_s}{\lambda_a})^4 \exp(-\frac{hc\nu}{kT}) \quad (5\text{-}1)$$

Where λ_s and λ_s are the Stokes and Anti-Stokes wavelengths, ν is the wavenumber separation from the pump wavelength, h is the Planck's constant, c is the velocity of light, k is the Boltzmann's constant, and T is the absolute temperature.

When a narrow pulse is injected into an optical fiber, continuous scattering will happen as the pulse travels to the other end. By filtering out the Anti-Stokes and Stokes components from the continuous waveform and taking the ratio of the two, the temperature profile along the fiber independent of laser intensity fluctuation can be acquired.

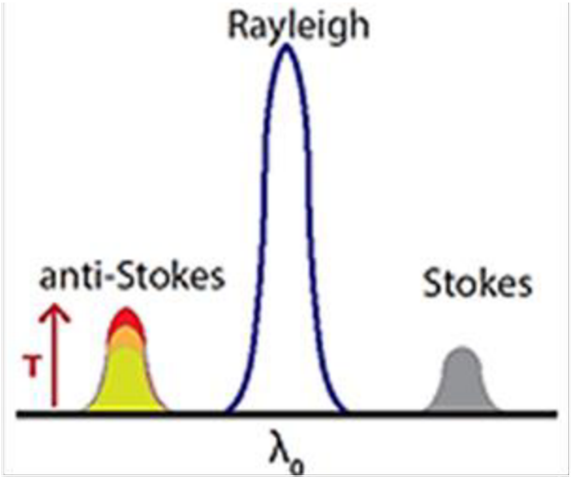

Figure 5-1 Raman scattering based temperature sensing principle

5.3 Result and Discussion

Multimode polymer optical fibers made from PC and PMMA were thermally drawn in the lab. In the visible range, the refractive index of PC and PMMA are 1.58 and 1.49 thus the light can be confined in the core made from PC. However, both materials were purchased from McMaster Carr and are not optical grade materials. Therefore the fiber loss is much larger than 10 dB/m and cannot be used here.

Commercial PMMA fiber (Paradigm Optics) used in this experiment has a 980 μm core made of PMMA, and the cladding is fluoropolymer with a lower refractive index 1.403. The overall fiber

diameter was 1 mm, and the numerical aperture is 0.5. The optical measurement was carried out with 5 m of the PMMA fiber, and the schematic of the Raman system is shown in **Figure 5-2 (a)**. Since the transmission window of PMMA is in the visible range, a 532 nm 700 ps laser was used, and the laser repetition rate was 2000 Hz. The laser was focused to the PMMA fiber, and the backscattered light passed through a notch filter centered at 532 nm to filter out the Rayleigh scattering signal. The return signal was first directly refocused to a CCD-based spectrometer (USB4000, Ocean optics) to observe the spectrum information. The CCD integration time was 3 s and the average number was 50. From the **Figure 5-2 (b)**, we can see the peak at 532 nm which is the residual Rayleigh scattering signal, and the Stokes and Anti-Stokes signals that are on each side. The Raman spectrum of PMMA has been reported, and the Stokes profile matches well with the reported results [95, 96]. The assignment of each peak is also given in the references. The strongest Stokes peak is at 2957 cm^{-1}(not shown in the figure), yet the corresponding Antistokes signal is too weak. Only the Anti-Stokes signal below 1000 cm^{-1} can be observed on the spectrometer. From the Stokes signal, we know that the region consists of five different peaks.

The return signal was then divided and passed two separate filters for Stokes and Anti-Stokes signal. The Stokes filter is a 25 nm FWHM bandpass filter centered at 550 nm, and the Anti-Stokes filter is a 25 mm FWHM bandpass filter center at 512 nm. A Si-based avalanche photodetectors (APD210 from Thorlabs) was used to pick up the pulses. The ratio of the Anti-Stokes signal and the Stokes signal are shown in **Figure 5-3 (a)**. Although the excitation pulse width is only 700 ps, the scattering occurred at every point along the 5 meters of fiber thus the return pulse lasted more than 40 ns. A 30 cm segment of the fiber was placed inside a box furnace, and the temperature was increased from room temperature to 86 ºC gradually. The ratio of the Anti-Stokes and Stokes signal has shown an increase in the middle, corresponding to the heated section. The temperature calibration curve is shown in **Figure 5-3 (b)**. Although the ratio follows an inverse exponential relationship given in Equation 5-1, in the small temperature range measured here it is almost linear. However, the Anti-Stokes signal from the PMMA fiber is very weak, and the accuracy of the data is expected to be inferior to traditional silica optical fiber.

Because the laser pulse width is 700 ps, the spatial resolution can be calculated to be 14 cm in this system.

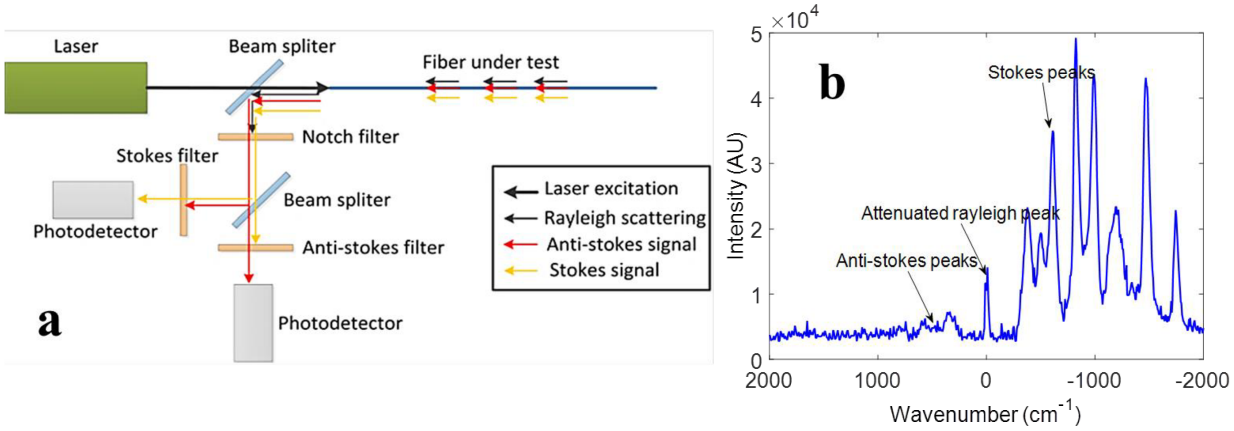

Figure 5-2 (a) Raman scattering based distributed temperature measurement system (b) Raman spectrum of the PMMA fiber measured with the system and a spectrometer

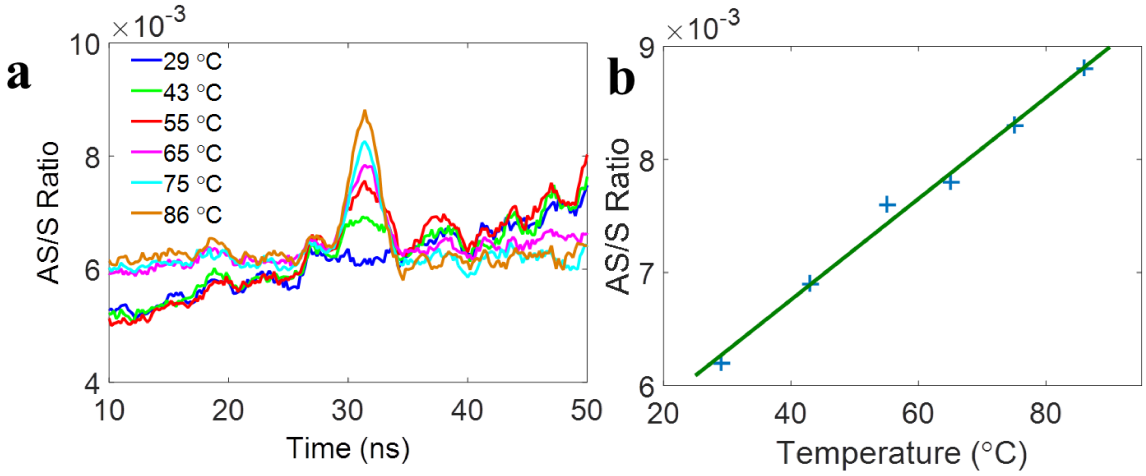

Figure 5-3 (a) Ratio of the Anti-Stokes and the Stokes intensity along the fiber when the middle section of the PMMA fiber was heated (b) the peak Anti-Stokes to Stokes ratio vs. temperature

Chapter 6 Porous Polymer Fiber

In this chapter, we reported the work on the fabrication of porous polymer fiber through controlling water concentration in PC and PMMA. The result has been published on Optical Materials Express, and I am the first author of the manuscript [97]. The figures in the publication are reproduced from the manuscript under fair use.

6.1 Review of Porous Fiber and Material Selection

Inspired by the previous random-hole silica optical fiber research conducted in the Center for Photonics Technology, Virginia Tech [98-101], we have investigated the possibility of fabricating porous polymer optical fibers. Two porosity generation mechanisms were used in the fabrication of the porous silica optical fibers. The first one is mixing a small percentage of gas-producing material such as silicon nitride and silica carbide with silica power in a silica tube [98]. The gas-producing materials oxidize during the high-temperature drawing and release gas to form bubbles in the glass preform. The bubbles are then drawn into long tubes, and the pore size in the drawn fiber ranging from 2.5 μm to tens of nanometers was reported [98]. The second method involves phase-separation of the cladding materials followed by leaching out the secondary phase, leaving a porous silica-rich structure [101]. The pore size is smaller (2 to 50 nm) compared to the ones made with gas producing agents [101]. The porosity in the fiber enables fast gas diffusion thus making the fiber ideal for gas sensing [100, 102].

Polymer materials have been used to make porous structures and porous fibers in particular. Porous fibers have been used for separation of gas, water and chemicals as well as tissue engineering [103-106]. Most of the porous polymer fibers are fabricated by spinning or extrusion and the intermediate fiber undergo phase separation for pore generation. Recently, Grena et al. have reported phase separation of a polymer solution during fiber thermal drawing and have presented fibers with pore sizes between 500 nm to 10 μm [71]. Aside from presenting porous fibers with different geometry and materials, they have demonstrated using the porous fiber to measure ionic conductivity of liquid filling the porous domain [71].

The pore generation principle reported here is similar to the one for random-hole silica optical fiber developed by Kominsky et al. [98] but the gas forming agent is the water in the polymer material. Some polymers commonly used for polymer fiber thermal drawing absorb water and require degassing in a vacuum oven to prevent pores formation when the preform made from the polymer is heated in the drawing tower. This is generally undesirable as the pores reduce the uniformity of the fiber and degrade optical and mechanical performance. We have taken the benefit of this process and shown that controlled and localized pore generation in fiber through water evaporation is possible.

For polymer materials used in this work, PC and PMMA have shown to retain water. 1 inch solid rods of PC and PMMA purchased from McMaster Carr and US plastics were first heated in a vacuum oven at 80 ºC for a week and the weight loss indicated that there were 0.09% and 0.18% w/w water in PC and PMMA. Different batches of the materials may have different residual water so we degas the materials before rehydrating them in water. Oven-dried PC and PMMA 1 inch rods were then immersed in deionized water and heated at 60 ºC. Their weight increase was monitored daily. The results shown in **Figure 6-1 (a)** suggests that PC can absorb water up to 0.5% percent of its weight while PMMA can absorb more than 2%. The result matches well with previous publication studying water in the two materials [107-109]. Inset photo of **Figure 6-1 (a)** also shows that PMMA rod has changed color from clear to milky white after long exposure to water. To study the pore formation temperature, PC and PMMA immersed in 60 ºC water for three days were heated in an oven at different temperatures in atmospheric pressure and in vacuum. We can draw two conclusions from the results shown **Figure 6-2 (b).** The environment pressure didn't change the outcome of the experiment as internal pressure from water evaporation would be the dominant factor. The onset temperature for pore generation for both polymers is around 180 ºC and all samples at and above the threshold show obvious formations of pores inside. The pores in the PC rod were smaller and more uniform; PMMA also showed a larger extent of deformation due to its lower glass transition temperature.

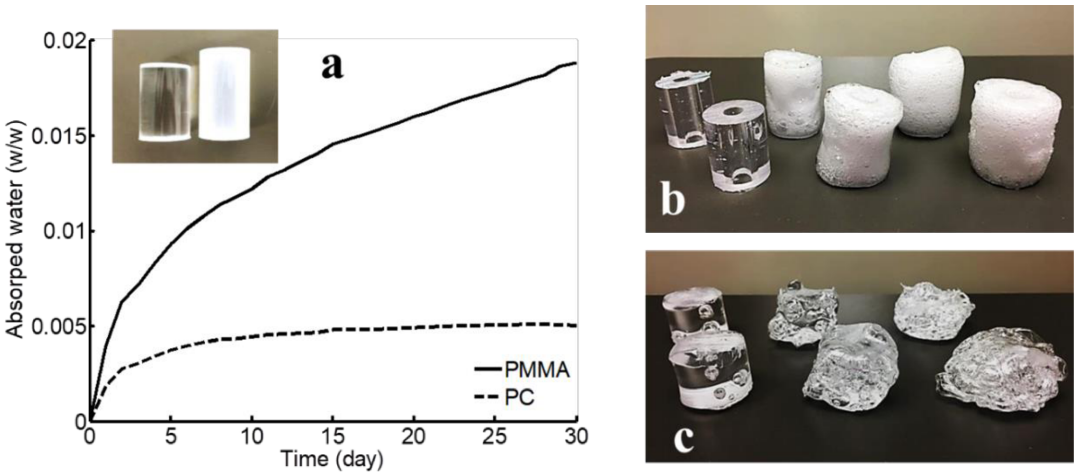

Figure 6-1 (a) Weight increase of PC and PMMA 1 inch rod immersed in 60 ºC water (inset: PMMA before (left) and after one-month water bath (right)) (b) and (c) PC and PMMA heated in oven for 30 minutes (in both figures front row: in vacuum, back row: in air; from left to right: temperature is 160 ºC, 180 ºC and 200 ºC). Figure reproduced from reference [97]

6.2 Fiber Drawing and Characterization

The thermal drawing technique for porous fiber fabrication is not different from drawing electrode-embedded polymer fibers discussed in previous chapters. The preform made with water-infused polymer was prepared in the lab before being drawn into fiber using the draw tower shown in **Figure 3-1**. The pore generation can happen during the drawing or before if the consolidation of the preform is needed and the consolidation temperature exceeds the 180 ºC threshold. We started by drawing 1 inch PC and PMMA rod that had been immersed in water at 60 ºC for three days (containing ~0.3% and ~0.7% w/w water), and we observed elongated pores along the fiber because a sphere pore in the preform would be elongated along the fiber draw direction. **Figure 3-2 (a)** shows a PC preform after drawing, and the pores can be observed in the heated region. To confine the porosity in a cladding of a fiber, a three-layer design was used in most preforms. A rod with no water content was inserted into a tube underwent the same three-day water treatment. A third outer layer of dry polymer was added to confine the porous region and provide additional support. This layer can be made with another tube matching the outer diameter of the first tube, or alternatively made by tightly wrapping PC or PMMA thin film and consolidate in vacuum. The three-layer preforms were then consolidated in vacuum oven to

eliminate the boundaries between each layer. If a preform only has PMMA, the consolidation can be carried out at 140 ºC; otherwise, 180 ºC is used. Note that the middle layer will become porous during the consolidation prior to the actual drawing if the consolidation temperature is 180 ºC. **Figure 6-2 (b)** and **(c)** show a three-layer pure PC preform with a porous middle layer after consolidation.

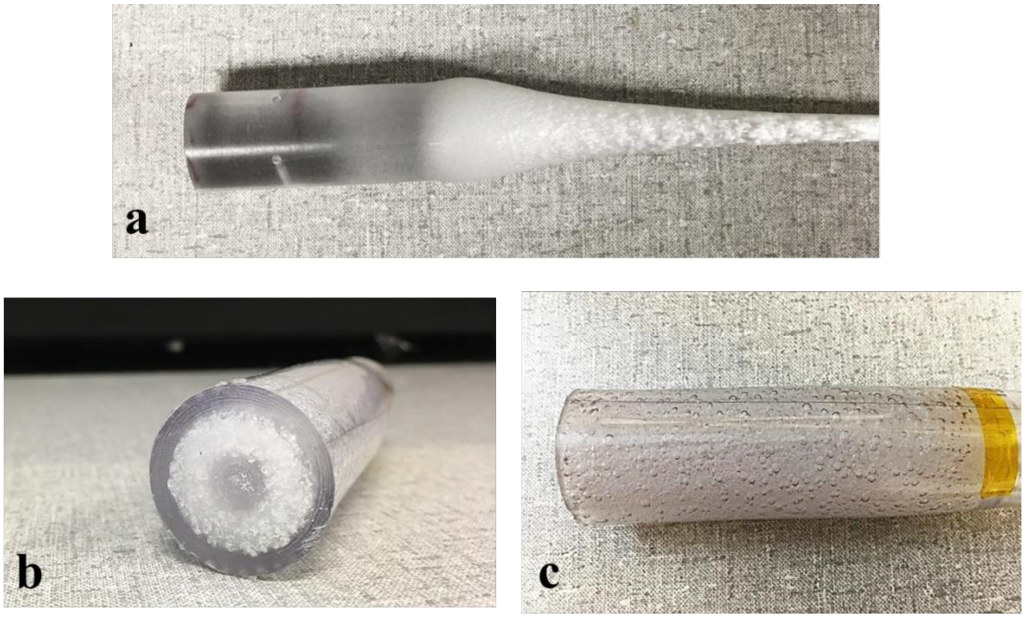

Figure 6-2 (a) 1 inch PC rod after thermal drawing showing porosity in heated region (b) PC three-layer preform after consolidation at 180 ºC (core diameter 0.25 inch, porous cladding diameter 0.75 inches, outer cladding dimeter 1inch)). Figure reproduced from reference [97]

As shown in **Figure 6-1**, pore generated in PMMA are larger and less uniform, and subsequent drawing of PMMA preform also yielded inferior porous fibers compared to the ones made from PC. Therefore the capillary tube drawing method was also adopted for PMMA. Capillaries were first drawn from tubes of vacuum-dried PMMA and were bundled around a solid PMMA core to serve as the middle layer. As the capillaries were drawn in the new preform, their diameters were reduced again.

Several fiber designs and draw condition combinations have been tested, and selected results are listed in Table 6-1 and **Figure 6-3**. The images were taken with an LEO 1550 field-emission SEM and PMMA fiber samples shown in **Figure 6-3 (c)** and **(d)** were cleaved with an RMC

Microtome machine after fixation in resin. The geometry of the preforms for Fiber A and B were the same, and the draw conditions were similar. The different porosity profile resulted from a higher water concentration in the preform for Fiber B (0.09% for A vs. 0.3% for B). It is suggested that lower water concentration leads to a more uniform pore distribution and a smaller pore size. Fiber C was made from PMMA and the majority of the pores on the fiber cross section were small and partially blocked by the resin used. Fiber D was drawn at a higher temperature, and some of the capillaries have collapsed due to its lower viscosity. Nevertheless, the middle porous region can be clearly identified.

	Preform material and geometry (dimension given in inch, the temperature is Celsius)				Drawing parameters	
	Material	Core	Cladding	Outer layer	Temperature	Final diameter (μm)
Fiber A	PC	0.25	0.75	1	265	400-900
Fiber B	PC	0.25	0.75	1	270	400-700
Fiber C	PMMA	0.5	0.75	1	210	400-700
Fiber D	PMMA	0.25	0.5	0.625	265	300-900

Table 6-1 Preform geometry and fiber drawing parameters, reproduced from reference [97]

The original design of the porous fiber was that the porous cladding would have a smaller average refractive index than the core, despite made with the same material. However, smaller pore size is required for the averaging effect to be dominant over scattering at the polymer/air boundary. We still measured the optical transmission loss of the four fibers using standard cutback methods, and the results are given in Table 6-2. The intrinsic material loss of the two materials is below 1 dB/m, and the polymers used here are not optical grade thus have much absorption and scattering loss than the theoretical value. Scattering at the polymer/air boundary also contributed to the overall loss of the fiber.

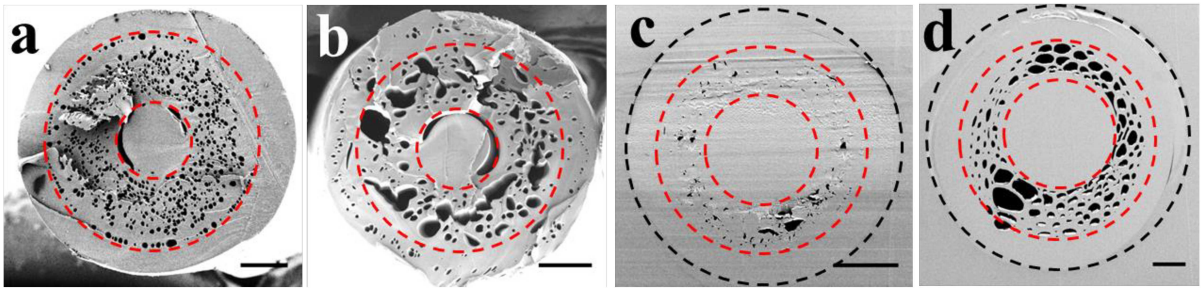

Figure 6-3 SEM images of the cross sections of porous fiber, red dash lines mark the porous region and the black dash line circles the fiber boundary, scale bar is 100 μm. Figure reproduced from reference [97]

	532 nm (dB/cm)	633 nm (dB/cm)
Fiber A	0.64	0.67
Fiber B	0.82	0.79
Fiber C	0.16	0.11
Fiber D	0.17	0.13

Table 6-2 Optical transmission loss of Fiber A-D, reproduced from reference [97]

To make an optic waveguide with better light confinement, a modified preform was made with PC and PMMA. The hybrid structure has a PC core, a PMMA cladding, and two PC outer claddings. The PC core and PMMA cladding constitute a polymer optical waveguide from the refractive index difference between the two materials. The middle PC cladding has water-induced pores, and the outer PC cladding supports the fiber structure. Although the porous region would not interact with the light guiding region directly, the fiber can be potentially used for local drug delivery with light activation. **Figure 6-4** shows images of the fiber cross section under SEM and optical microscope.

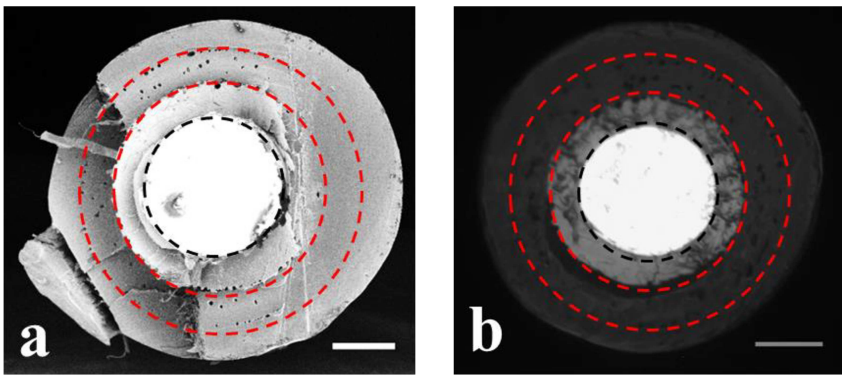

Figure 6-4 (a) SEM image of the cross section of porous fiber made from PC and PMMA (b) Optical microscopic image of the porous fiber with light injected to the core region from the other end. Scale bar is 100 μm. Figure reproduced from reference [97]

6.3 Proof-of-concept Demonstration of Drug Release by Porous Fibers

The capillaries in the porous region of the polymer are capable of absorbing liquid, and this can facilitate broad applications in the biomedical field. We have shown that the fiber can be potentially used for localized drug delivery.

Photosensitive drugs have been used in photodynamic therapy for cancer treatments [110, 111]. The drugs can induce cell death in the cancer region with localized light activation. When the drug is given intravenously, one limitation is that the patient needs to limit exposure to light to avoid systematic toxicity. Special fibers with both drug delivery and light activation function can overcome this limitation and offer a compact solution for treatment in deep tissue. Photosensitive drugs can be loaded to the porous region of the fiber by capillary force in advance and be released to the patient after fiber implant. The same fiber can then activate the drug locally with its light guiding capability.

We have simulated the drug release process by loading porous fibers with a fluorescent dye and have recorded dye diffusion to tissue phantom and live tumors. The experiments were in collaboration with Dr. Xiaoting Jia's group and Dr. Rong Tong's group at Virginia Tech. The dye used in the experiment was rhodamine dissolved in water (2 mg/mL) which emits red light with green light excitation. Three types of fiber (porous PC fiber, porous PMMA fiber, capillary PMMA fiber) were dipped in the dye solution for loading. The treated fiber were dried overnight and inserted to agarose gel blocks immersed in phosphate buffered saline. The fiber and the gel were kept at 37 ℃ and fluorescent images taken by IVIS imaging systems after two days have confirmed the dye diffusion from fiber to the phantom tissue shown in Figure 6-5 (a). Similar results were observed in ex vivo experiments in which we inserted the fiber to murine 4T1 mammary tumors. The qualitative results have paved roads for sustained and controlled drug release and activation via functional porous polymer optical fiber.

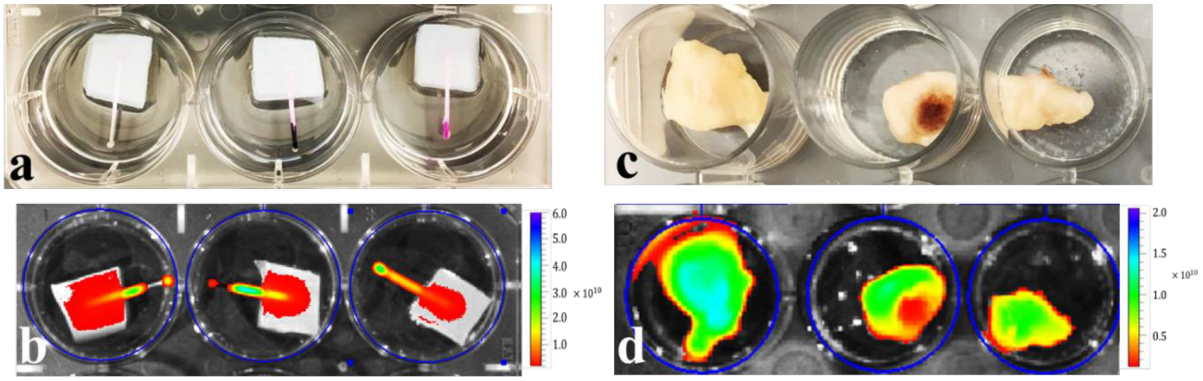

Figure 6-5 (a) Photo of agarose gel blocks with inserted porous polymer fiber (b) Fluorescent image showing dye release from fiber to the gel shown in (a) (c) Photo of murine 4T1 tumors used in the simulated drug release test (d) Fluorescent image of dye released in tumors in (c) The color in (b) & (d) is presented as the radiant efficiency. In all figures, from left to right test subjects were inserted with the porous-cladding PC fiber, the capillary tube-cladding PMMA fiber and the porous-cladding PMMA fiber. Figure reproduced from reference [97]

Chapter 7 Summary

The work presented in this dissertation is focused on the development of novel polymer fiber devices fabricated by thermal drawing and the implementation of polymer fiber-based distributed sensors. The project was divided into three major sections.

First, we have reported research progress in combining functional polymer fibers fabricated by thermal drawing with electrical reflectometry. The flexibility of the thermal drawing technique allows different materials to be incorporated together, enabling complex sensor structure to be made within a fiber preform. The preform can then be drawn into submillimeter fiber that maintains the same structure on a much smaller scale. With the help of convergence drawing, low resistance metal electrodes have been successfully embedded inside polymer fibers to form continuous sensing elements. Polymer fibers with embedded electrodes have been designed and fabricated for distributed temperature and pressure sensing. The temperature sensing principle is the impedance change from thermal expansion or permittivity change of the polymer material between the electrodes. Impedance change from deformation of thermoplastic elastomer material between the electrodes was used for pressure sensing. The temperature resolution of the LDPE fiber and the PVDF fiber can reach 2°C. The pressure sensing fiber with thermoplastic elastomer between the two copper electrodes can detect pressure between 10-60 kPa.

Secondly, we have implemented a Raman distributed temperature sensing system with commercial PMMA polymer optical fibers. Raman scattering based temperature sensor provides a distributed sensing solution immune to electrical magnetic interference and the laser intensity fluctuation. The ratio of Anti-Stokes and Stokes backscattering intensity from the PMMA fiber recorded with high-speed avalanche photodetectors show a quasi-linear relationship with temperature. A theoretical spatial resolution of 14 cm can be achieved with the sub-nanosecond pulse laser used in the interrogation system.

Lastly, we have explored the possibility of thermally drawing porous polymer fiber from polymer materials with a controlled water concentration. The evaporation of water generates pores that are elongated along the fiber axial direction during drawing. The fibers allow liquid to

be drawn into the porous region and proof-of-concept drug release experiments on tissue phantom and murine tumors have demonstrated the potential for the porous fiber to be used for localized drug delivery and activation.

Reference

[1] H. Gooding, “Cable-fault location on power systems,” *Proceedings of the Institution of Electrical Engineers*, vol. 113, no. 1, p. 111, 1966.

[2] B. Clegg and N. Lord, “Modern cable-fault-location methods,” *Proceedings of the Institution of Electrical Engineers*, vol. 122, no. 4, p. 395, 1975.

[3] C. H. Dowding, M. B. Su, and K. Oconnor, “Measurement of rock mass deformation with grouted coaxial antenna cables,” *Rock Mechanics and Rock Engineering*, vol. 22, no. 1, pp. 1–23, 1989.

[2] C. H. Dowding and F. C. Huang, “Early Detection of Rock Movement with Time Domain Reflectometry,” *Journal of Geotechnical Engineering*, vol. 120, no. 8, pp. 1413–1427, 1994.

[5] S, John, K Thuro, and U. Sambeth. "Development of a continuous 3d-monitoring system for unstable slopes using time domain reflectometry." IAEG2006 .

[6] R. Greco, “Soil water content inverse profiling from single TDR waveforms,” *Journal of Hydrology*, vol. 317, no. 3-4, pp. 325–339, 2006.

[7] M. W. Lin, A. O. Abatan, and W.-M. Zhang, “,” *Smart Structures and Materials 1998: Smart Systems for Bridges, Structures, and Highways*, 1998.

[8] M. W. Lin, A. O. Abatan, and Y. Zhou, “High-sensitivity electrical TDR distributed strain sensor,” *Smart Structures and Materials 2000: Sensory Phenomena and Measurement Instrumentation for Smart Structures and Materials*, Dec. 2000.

[9] B. Lee, “Review of the present status of optical fiber sensors,” *Optical Fiber Technology*, vol. 9, no. 2, pp. 57–79, 2003.

[10] O. S. Wolfbeis, “Fiber-Optic Chemical Sensors and Biosensors,” Analytical Chemistry, vol. 78, no. 12, pp. 3859–3874, 2006.

[11] L. Ma, C. Ma, Y. Wang, D. Y. Wang, and A. Wang, “High-Speed Distributed Sensing Based on Ultra Weak FBGs and Chromatic Dispersion,” *IEEE Photonics Technology Letters*, vol. 28, no. 12, pp. 1344–1347, 2016.

[12] Y. Wang, J. Gong, B. Dong, D. Y. Wang, T. J. Shillig, and A. Wang, “A Large Serial Time-Division Multiplexed Fiber Bragg Grating Sensor Network,” *Journal of Lightwave Technology*, vol. 30, no. 17, pp. 2751–2756, 2012.

[13] A. Hartog, A. Leach, and M. Gold, “Distributed temperature sensing in solid-core fibres,” *Electronics Letters*, vol. 21, no. 23, p. 1061, 1985.

[14] M. Niklès, L. Thévenaz, and P. A. Robert, “Simple distributed fiber sensor based on Brillouin gain spectrum analysis,” *Optics Letters*, vol. 21, no. 10, p. 758, 1996.

[15] B. J. Soller, D. K. Gifford, M. S. Wolfe, and M. E. Froggatt, “High resolution optical frequency domain reflectometry for characterization of components and assemblies,” *Optics Express*, vol. 13, no. 2, p. 666, 2005.

[16] A. Minardo, R. Bernini, and L. Zeni, “Distributed Temperature Sensing in Polymer Optical Fiber by BOFDA,” *IEEE Photonics Technology Letters*, vol. 26, no. 4, pp. 387–390, 2014.

[17] S. T. Kreger, A. K. Sang, D. K. Gifford, and M. E. Froggatt, "Distributed strain and temperature sensing in plastic optical fiber using Rayleigh scatter," *Fiber Optic Sensors and Applications VI*, Jan. 2009..

[18] S. Liehr, P. Lenke, M. Wendt, K. Krebber, M. Seeger, E. Thiele, H. Metschies, B. Gebreselassie, and J. Munich, "Polymer Optical Fiber Sensors for Distributed Strain Measurement and Application in Structural Health Monitoring," *IEEE Sensors Journal*, vol. 9, no. 11, pp. 1330–1338, 2009.

[19] J. S. Heo, J. Eom, Y.-H. Kim, and S. K. Park, "Recent Progress of Textile-Based Wearable Electronics: A Comprehensive Review of Materials, Devices, and Applications," *Small*, vol. 14, no. 3, p. 1703034, Apr. 2017.

[20] W. Weng, P. Chen, S. He, X. Sun, and H. Peng Smart electronic textiles. *Angewandte Chemie International Edition*, p.6140-6169. (2016).

[21] B. Oconnor, K. H. An, Y. Zhao, K. P. Pipe, and M. Shtein, "Fiber Shaped Light Emitting Device," *Advanced Materials*, vol. 19, no. 22, pp. 3897–3900, 2007.

[22] S. Lee, S. Shin, S. Lee, J. Seo, J. Lee, S. Son, H. J. Cho, H. Algadi, S. Al-Sayari, D. E. Kim, and T. Lee, "Stretchable Electronics: Ag Nanowire Reinforced Highly Stretchable Conductive Fibers for Wearable Electronics (Adv. Funct. Mater. 21/2015)," *Advanced Functional Materials*, vol. 25, no. 21, pp. 3105–3105, 2015.

[23] Z. Yang, J. Deng, X. Sun, H. Li, and H. Peng, "Stretchable, Wearable Dye-Sensitized Solar Cells," *Advanced Materials*, vol. 26, no. 17, pp. 2643–2647, 2014.

[24] M. Rein, V. D. Favrod, C. Hou, T. Khudiyev, A. Stolyarov, J. Cox, C.-C. Chung, C. Chhav, M. Ellis, J. Joannopoulos, and Y. Fink, "Diode fibres for fabric-based optical communications," *Nature*, vol. 560, no. 7717, pp. 214–218, 2018.

[25] M. R. Lee, R. D. Eckert, K. Forberich, G. Dennler, C. J. Brabec, and R. A. Gaudiana, "Solar Power Wires Based on Organic Photovoltaic Materials," *Science*, vol. 324, no. 5924, pp. 232–235, Oct. 2009.

[26] T. L. Andrew, L. Zhang, N. Cheng, M. Baima, J. J. Kim, L. Allison, and S. Hoxie, "Melding Vapor-Phase Organic Chemistry and Textile Manufacturing To Produce Wearable Electronics," *Accounts of Chemical Research*, vol. 51, no. 4, pp. 850–859, Sep. 2018.

[27] Z. Yang, H. Sun, T. Chen, L. Qiu, Y. Luo, and H. Peng, "Photovoltaic Wire Derived from a Graphene Composite Fiber Achieving an 8.45 % Energy Conversion Efficiency," *Angewandte Chemie*, vol. 125, no. 29, pp. 7693–7696, 2013.

[28] Y. Guo, X.-S. Zhang, Y. Wang, W. Gong, Q. Zhang, H. Wang, and J. Brugger, "All-fiber hybrid piezoelectric-enhanced triboelectric nanogenerator for wearable gesture monitoring," *Nano Energy*, vol. 48, pp. 152–160, 2018.

[29] A. F. Abouraddy, M. Bayindir, G. Benoit, S. D. Hart, K. Kuriki, N. Orf, O. Shapira, F. Sorin, B. Temelkuran, and Y. Fink, "Towards multimaterial multifunctional fibres that see, hear, sense and communicate," *Nature Materials*, vol. 6, no. 5, pp. 336–347, 2007.

[30] G. Tao, A. M. Stolyarov, and A. F. Abouraddy, "Multimaterial Fibers," *International Journal of Applied Glass Science*, vol. 3, no. 4, pp. 349–368, 2012.

[31] W. Yan, A. Page, T. Nguyen-Dang, Y. Qu, F. Sordo, L. Wei, and F. Sorin, "Advanced Multimaterial Electronic and Optoelectronic Fibers and Textiles," *Advanced Materials*, p. 1802348, Nov. 2018.

[32] Y. Fink, “A Dielectric Omnidirectional Reflector,” *Science*, vol. 282, no. 5394, pp. 1679–1682, 1998.

[33] S. D. Hart, “External Reflection from Omnidirectional Dielectric Mirror Fibers,” *Science*, vol. 296, no. 5567, pp. 510–513, 2002.

[34] O. Shapira, K. Kuriki, N. D. Orf, A. F. Abouraddy, G. Benoit, J. F. Viens, A. Rodriguez, M. Ibanescu, J. D. Joannopoulos, Y. Fink, and M. M. Brewster, “Surface-emitting fiber lasers,” *Optics Express*, 2006.

[35] M. Bayindir, F. Sorin, A. F. Abouraddy, J. Viens, S. D. Hart, J. D. Joannopoulos, and Y. Fink, “Metal–insulator–semiconductor optoelectronic fibres,” *Nature*, vol. 431, no. 7010, pp. 826–829, 2004.

[36] M. Bayindir, A. F. Abouraddy, J. Arnold, J. D. Joannopoulos, and Y. Fink, “Thermal-Sensing Fiber Devices by Multimaterial Codrawing,” *Advanced Materials*, vol. 18, no. 7, pp. 845–849, Apr. 2006.

[37] S. Egusa, Z. Wang, N. Chocat, Z. M. Ruff, A. M. Stolyarov, D. Shemuly, F. Sorin, P. T. Rakich, J. D. Joannopoulos, and Y. Fink, “Multimaterial piezoelectric fibres,” *Nature Materials*, vol. 9, no. 8, pp. 643–648, Nov. 2010.

[38] T. Khudiyev, J. Clayton, E. Levy, N. Chocat, A. Gumennik, A. M. Stolyarov, J. Joannopoulos, and Y. Fink, “Electrostrictive microelectromechanical fibres and textiles,” *Nature Communications*, vol. 8, no. 1, Oct. 2017.

[39] T. Khudiyev, C. Hou, A. M. Stolyarov, and Y. Fink, “Surface Patterning: Sub-Micrometer Surface-Patterned Ribbon Fibers and Textiles (Adv. Mater. 22/2017),” *Advanced Materials*, vol. 29, no. 22, 2017.

[40] G. Lestoquoy, N. Chocat, Z. Wang, J. D. Joannopoulos, and Y. Fink, “Fabrication and characterization of thermally drawn fiber capacitors,” *Applied Physics Letters*, vol. 102, no. 15, p. 152908, 2013.

[41] Y. Qu, T. Nguyen-Dang, A. G. Page, W. Yan, T. D. Gupta, G. M. Rotaru, R. M. Rossi, V. D. Favrod, N. Bartolomei, and F. Sorin, “Superelastic Multimaterial Electronic and Photonic Fibers and Devices via Thermal Drawing,” *Advanced Materials*, vol. 30, no. 27, p. 1707251, 2018.

[42] A. Gumennik, A. M. Stolyarov, B. R. Schell, C. Hou, G. Lestoquoy, F. Sorin, W. Mcdaniel, A. Rose, J. D. Joannopoulos, and Y. Fink, “All-in-Fiber Chemical Sensing,” *Advanced Materials*, vol. 24, no. 45, pp. 6005–6009, Feb. 2012.

[43] A. F. Abouraddy, O. Shapira, M. Bayindir, J. Arnold, F. Sorin, D. S. Hinczewski, J. D. Joannopoulos, and Y. Fink, “Large-scale optical-field measurements with geometric fibre constructs,” *Nature Materials*, vol. 5, no. 7, pp. 532–536, 2006.

[44] A. Canales, X. Jia, U. P. Froriep, R. A. Koppes, C. M. Tringides, J. Selvidge, C. Lu, C. Hou, L. Wei, Y. Fink, and P. Anikeeva, “Multifunctional fibers for simultaneous optical, electrical and chemical interrogation of neural circuits in vivo,” *Nature Biotechnology*, vol. 33, no. 3, pp. 277–284, 2015.

[45] S. Park, Y. Guo, X. Jia, H. K. Choe, B. Grena, J. Kang, J. Park, C. Lu, A. Canales, R. Chen, Y. S. Yim, G. B. Choi, Y. Fink, and P. Anikeeva, “One-step optogenetics with multifunctional flexible polymer fibers,” *Nature Neuroscience*, vol. 20, no. 4, pp. 612–619, 2017.

[46] R. A. Koppes, S. Park, T. Hood, X. Jia, N. A. Poorheravi, A. H. Achyuta, Y. Fink, and P. Anikeeva, “Thermally drawn fibers as nerve guidance scaffolds,” *Biomaterials*, vol. 81, pp. 27–35, 2016.

[47] B. Temelkuran, S. D. Hart, G. Benoit, J. D. Joannopoulos, and Y. Fink, “Wavelength-scalable hollow optical fibres with large photonic bandgaps for CO2 laser transmission,” *Nature*, vol. 420, no. 6916, pp. 650–653, 2002.

[48] S. Shabahang, F. A. Tan, J. D. Perlstein, G. Tao, O. Alvarez, F. Chenard, A. Sincore, L. Shah, M. C. Richardson, K. L. Schepler, and A. F. Abouraddy, “Robust multimaterial chalcogenide fibers produced by a hybrid fiber-fabrication process,” *Optical Materials Express*, vol. 7, no. 7, p. 2336, Sep. 2017.

[49] S. Peng, G. Tang, K. Huang, Q. Qian, D. Chen, Q. Zhang, and Z. Yang, Crystalline selenium core optical fibers with low optical loss. *Optical Materials Express*, pp.1804-1812. 2017.

[50] J. R. Sparks, R. He, N. Healy, M. Krishnamurthi, A. C. Peacock, P. J. A. Sazio, V. Gopalan, and J. V. Badding, “Zinc Selenide Optical Fibers,” *Advanced Materials*, vol. 23, no. 14, pp. 1647–1651, Jan. 2011.

[51] M. Yaman, T. Khudiyev, E. Ozgur, M. Kanik, O. Aktas, E. O. Ozgur, H. Deniz, E. Korkut, and M. Bayindir, “Arrays of indefinitely long uniform nanowires and nanotubes,” *Nature Materials*, vol. 10, no. 9, pp. 722–722, 2011.

[52] J. J. Kaufman, G. Tao, S. Shabahang, D. S. Deng, Y. Fink, and A. F. Abouraddy, “Thermal Drawing of High-Density Macroscopic Arrays of Well-Ordered Sub-5-nm-Diameter Nanowires,” *Nano Letters*, vol. 11, no. 11, pp. 4768–4773, Sep. 2011.

[53] J. J. Kaufman, G. Tao, S. Shabahang, E.-H. Banaei, D. S. Deng, X. Liang, S. G. Johnson, Y. Fink, and A. F. Abouraddy, “Structured spheres generated by an in-fibre fluid instability,” *Nature*, vol. 487, no. 7408, pp. 463–467, 2012.

[54] J. J. Kaufman, R. Ottman, G. Tao, S. Shabahang, E.-H. Banaei, X. Liang, S. G. Johnson, Y. Fink, R. Chakrabarti, and A. F. Abouraddy, “In-fiber production of polymeric particles for biosensing and encapsulation,” *Proceedings of the National Academy of Sciences*, vol. 110, no. 39, pp. 15549–15554, Sep. 2013.

[55] C. Hou, X. Jia, L. Wei, S.-C. Tan, X. Zhao, J. D. Joannopoulos, and Y. Fink, “Crystalline silicon core fibres from aluminium core preforms,” *Nature Communications*, vol. 6, no. 1, 2015.

[56] C. Hou and Y. Fink, “Fiber Draw Synthesis,” *Asia Communications and Photonics Conference 2014*, 2014.

[57] T. Nguyen-Dang, A. G. Page, Y. Qu, M. Volpi, W. Yan, and F. Sorin, “Multi-material micro-electromechanical fibers with bendable functional domains,” *Journal of Physics D: Applied Physics*, vol. 50, no. 14, p. 144001, Jul. 2017.

[58] D. M. Pozar, *Microwave engineering*. Wiley, 2017.

[59] Y. Ohki, T. Yamada and N. Hirai, “Precise location of the excessive temperature points in polymer insulated cables,” *IEEE Transactions on Dielectrics and Electrical Insulation*, vol. 20, no. 6, pp. 2099–2106, 2013.

[60] R. Cole, "Time domain reflectometry." *Annual review of physical chemistry* p. 283-300 1977.

[61] C. Furse, Y. C. Chung, R. Dangol, M. Nielsen, G. Mabey, and R. Woodward, “Frequency-domain reflectometery for on-board testing of aging aircraft wiring,” *IEEE Transactions on Electromagnetic Compatibility*, vol. 45, no. 2, pp. 306–315, 2003.

[62] J. Huang, X. Lan, W. Zhu, B. Cheng, J. Fan, Z. Zhou, and H. Xiao, "Interferogram Reconstruction of Cascaded Coaxial Cable Fabry-Perot Interferometers for Distributed Sensing Application," *IEEE Sensors Journal*, vol. 16, no. 11, pp. 4495–4500, 2016.

[63] Y. Chung, C. Furse, and J. Pruitt, "Application of Phase Detection Frequency Domain Reflectometry for Locating Faults in an F-18 Flight Control Harness," *IEEE Transactions on Electromagnetic Compatibility*, vol. 47, no. 2, pp. 327–334, 2005.

[64] M. Beckers, T. Schlüter, T. Vad, T. Gries, and C.-A. Bunge, "An overview on fabrication methods for polymer optical fibers," *Polymer International*, vol. 64, no. 1, pp. 25–36, Jan. 2014.

[65] S. Chen, T. Huang, H. Zuo, S. Qian, Y. Guo, L. Sun, D. Lei, Q. Wu, B. Zhu, C. He, X. Mo, E. Jeffries, H. Yu, and Z. You, "Wearable Electronics: A Single Integrated 3D-Printing Process Customizes Elastic and Sustainable Triboelectric Nanogenerators for Wearable Electronics (Adv. Funct. Mater. 46/2018)," *Advanced Functional Materials*, vol. 28, no. 46, p. 1870331, 2018.

[66] K. Oh and U.-C. Paek, *Silica optical fiber technology for devices and components: design, fabrication, and international standards*. Hoboken, NJ: Wiley, 2012.

[67] M. Becker, M. Werner, O. Fitzau, D. Esser, J. Kobelke, A. Lorenz, A. Schwuchow, M. Rothhardt, K. Schuster, D. Hoffmann, and H. Bartelt, "Laser-drilled free-form silica fiber preforms for microstructured optical fibers," *Optical Fiber Technology*, vol. 19, no. 5, pp. 482–485, 2013.

[68] P. Zhang, J. Zhang, P. Yang, S. Dai, X. Wang, and W. Zhang, "Fabrication of chalcogenide glass photonic crystal fibers with mechanical drilling," *Optical Fiber Technology*, vol. 26, pp. 176–179, 2015.

[69] P. Toal, L. Holmes, R. Rodriguez, and E. Wetzel, "Microstructured monofilament via thermal drawing of additively manufactured preforms," *Additive Manufacturing*, vol. 16, pp. 12–23, 2017.

[70] K. Cook, G. Balle, J. Canning, L. Chartier, T. Athanaze, M. A. Hossain, C. Han, J.-E. Comatti, Y. Luo, and G.-D. Peng, "Step-index optical fiber drawn from 3D printed preforms," *Optics Letters*, vol. 41, no. 19, p. 4554, 2016.

[71] B. Grena, J.-B. Alayrac, E. Levy, A. M. Stolyarov, J. D. Joannopoulos, and Y. Fink, "Thermally-drawn fibers with spatially-selective porous domains," *Nature Communications*, vol. 8, no. 1, 2017.

[72] M. Amjadi, Y. J. Yoon, and I. Park, "Ultra-stretchable and skin-mountable strain sensors using carbon nanotubes–Ecoflex nanocomposites," *Nanotechnology*, vol. 26, no. 37, p. 375501, 2015.

[73] R. Matsuzaki and K. Tabayashi, "Wearables: Highly Stretchable, Global, and Distributed Local Strain Sensing Line Using GaInSn Electrodes for Wearable Electronics (Adv. Funct. Mater. 25/2015)," Advanced Functional Materials, vol. 25, no. 25, pp. 3797–3797, 2015.

[74] G. Wypych, *Handbook of polymers*. Toronto: Elsevier, ChemTec Publishing, 2016.

[75] V. Svorčík, E. Ondřej, V. Rybka, J. Lipták and V. Hnatowicz, "Permittivity of polyethylene and polyethyleneterephtalate". *Journal of Materials Science* p.1843-1845. 2000.

[76] V. Švorčík, J. Králová, V. Rybka, J. Plešek, J. Červená, and V. Hnatowicz, "Temperature dependence of the permittivity of polymer composites," *Journal of Polymer Science Part B: Polymer Physics*, vol. 39, no. 8, pp. 831–834, 2001.

[77] V. Švorčík, T. Podgrabinski, J. Náhlík, V. Rybka, and V. Hnatowicz, "Dielectric properties of doped polymethylmethacrylate," *Materials Letters*, vol. 59, no. 2-3, pp. 341–344, 2005.

[78] V. S. Yadav, D. K. Sahu, Y. Singh, M. Kumar, D. C. Dhubkarya, S.-I. Ao, H. Katagir, L. Xu, and A. H.-S. Chan, "Frequency and Temperature Dependence of Dielectric Properties of Pure Poly Vinylidene Fluoride (PVDF) Thin Films," 2010.

[79] J. Mark, *Physical properties of polymers handbook*. Springer, 2007.

[80] https://www.allaboutcircuits.com/tools/microstrip-impedance-calculator/

[81] J. P. Dakin, D. J. Pratt, G. W. Bibby, and J. N. Rose, "Distributed antistokes ratio thermometry," *Optical Fiber Sensors*, 1985.

[82] B. Liu, Z. Yu, C. Hill, Y. Cheng, D. Homa, G. Pickrell, and A. Wang, "Sapphire-fiber-based distributed high-temperature sensing system," *Optics Letters*, vol. 41, no. 18, p. 4405, 2016.

[83] W. Daum, *POF-Polymer optical fibers for data communication*. Berlin: Springer, 2002.

[84] M. G. Kuzyk, *Polymer fiber optics: materials, physics, and applications*. Boca Raton, FL: CRC/Taylor & Francis, 2007.

[85] M. Large, *Microstructured polymer optical fibres*. Springer, 2014.

[86] J. Hecht, *Understanding fiber optics*. Auburndale, MA: Laser Light Press, 2015.

[87] P. Polishuk, "Plastic optical fibers branch out," *IEEE Communications Magazine*, vol. 44, no. 9, pp. 140–148, 2006.

[88] Van Eijkelenborg, M.A., Large, M.C., Argyros, A., Zagari, J., Manos, S., Issa,., Bassett, I., Fleming, S., McPhedran, R.C., de Sterke, C.M. and Nicorovici,., "Microstructured polymer optical fibre." *Optics express*, pp.319-327.2001

[89] A. Grillet, D. Kinet, J. Witt, M. Schukar, K. Krebber, F. Pirotte, and A. Depre, "Optical Fiber Sensors Embedded Into Medical Textiles for Healthcare Monitoring," *IEEE Sensors Journal*, vol. 8, no. 7, pp. 1215–1222, 2008.

[90] I. R. Husdi, K. Nakamura, and S. Ueha, "Sensing characteristics of plastic optical fibres measured by optical time-domain reflectometry," *Measurement Science and Technology*, vol. 15, no. 8, pp. 1553–1559, 2004.

[91] S. Liehr, N. Nöther, and K. Krebber, "Incoherent optical frequency domain reflectometry and distributed strain detection in polymer optical fibers," *Measurement Science and Technology*, vol. 21, no. 1, p. 017001, 2009.

[92] Y. Mizuno and K. Nakamura, "Experimental study of Brillouin scattering in perfluorinated polymer optical fiber at telecommunication wavelength," *Applied Physics Letters*, vol. 97, no. 2, p. 021103, Dec. 2010.

[93] N. Hayashi, Y. Mizuno, and K. Nakamura, "Brillouin gain spectrum dependence on large strain in perfluorinated graded-index polymer optical fiber," *Optics Express*, vol. 20, no. 19, p. 21101, 2012.

[94] J. Dakin, D. Pratt, G. Bibby, and J. Ross, "Distributed optical fibre Raman temperature sensor using a semiconductor light source and detector," *Electronics Letters*, vol. 21, no. 13, p. 569, 1985.

[95] X. Xingsheng, M. Hai, Z. Qijing, and Z. Yunsheng, "Properties of Raman spectra and laser-induced birefringence in polymethyl methacrylate optical fibres," *Journal of Optics A: Pure and Applied Optics*, vol. 4, no. 3, pp. 237–242, Jul. 2002.

[96] K. J. Thomas, M. Sheeba, V. P. N. Nampoori, C. P. G. Vallabhan, and P. Radhakrishnan, "Raman spectra of polymethyl methacrylate optical fibres excited by a 532 nm diode pumped solid state laser," *Journal of Optics A: Pure and Applied Optics*, vol. 10, no. 5, p. 055303, 2008.

[97] L. Yu, H. Xuan, Y. Guo, A. L. Chin, R. Tong, G. Pickrell, A. Wang, and X. Jia, "Porous polymer optical fiber fabrication and potential biomedical application," *Optical Materials Express*, vol. 7, no. 6, p. 1813, Nov. 2017.

[98] D. Kominsky, G. Pickrell, and R. Stolen, "Generation of random-hole optical fiber," *Optics Letters*, vol. 28, no. 16, p. 1409, 2003.

[99] G. Pickrell, N. Manjooran, N. Goel, and D. Kominsky, "Silicon induced in situ hole formation in optical fibers," *Journal of Non-Crystalline Solids*, vol. 352, no. 6-7, pp. 500–504, 2006.

[100] C. Ma, B. Scott, G. Pickrell, and A. Wang, "Porous capillary tubing waveguide for multigas sensing," *Optics Letters*, vol. 35, no. 3, p. 315, 2010.

[101] B. Scott, C. Ma, G. Pickrell, K. Cooper, A. Wang, and T. Ooi, "Novel chemical and biological fiber optic sensor," *Micro (MEMS) and Nanotechnologies for Defense and Security*, 2007.

[102] G. Pickrell, W. Peng, and A. Wang, "Random-hole optical fiber evanescent-wave gas sensing," *Optics Letters*, vol. 29, no. 13, p. 1476, Jan. 2004.

[103] Y. Li, C. Cao, T.-S. Chung, and K. P. Pramoda, "Fabrication of dual-layer polyethersulfone (PES) hollow fiber membranes with an ultrathin dense-selective layer for gas separation," *Journal of Membrane Science*, vol. 245, no. 1-2, pp. 53–60, 2004.

[104] K. Y. Wang, T.-S. Chung, and M. Gryta, "Hydrophobic PVDF hollow fiber membranes with narrow pore size distribution and ultra-thin skin for the fresh water production through membrane distillation," *Chemical Engineering Science*, vol. 63, no. 9, pp. 2587–2594, 2008.

[105] Q. Yang, T.-S. Chung, and Y. Santoso, "Tailoring pore size and pore size distribution of kidney dialysis hollow fiber membranes via dual-bath coagulation approach," *Journal of Membrane Science*, vol. 290, no. 1-2, pp. 153–163, Jan. 2007.

[106] X. Wen and P. Tresco, "Fabrication and characterization of permeable degradable poly(dl-lactide-co-glycolide) (PLGA) hollow fiber phase inversion membranes for use as nerve tract guidance channels," *Biomaterials*, vol. 27, no. 20, pp. 3800–3809, 2006.

[107] M. N'Diaye, F. Pascaretti-Grizon, P. Massin, M. F. Baslé, and D. Chappard, "Water Absorption of Poly(methyl methacrylate) Measured by Vertical Interference Microscopy," *Langmuir*, vol. 28, no. 31, pp. 11609–11614, 2012.

[108] G. Baschek, G. Hartwig, and F. Zahradnik, "Effect of water absorption in polymers at low and high temperatures," *Polymer*, vol. 40, no. 12, pp. 3433–3441, 1999.

[109] E. Ito and Y. Kobayashi, "Changes in physical properties of polycarbonate by absorbed water," *Journal of Applied Polymer Science*, vol. 22, no. 4, pp. 1143–1149, 1978.

[110] D. Dolmans, D. Fukumura and R. Jain. Photodynamic therapy for cancer. *Nature reviews cancer*, p.380. 2003

[111] S. Mallidi, S. Anbil, A.-L. Bulin, G. Obaid, M. Ichikawa, and T. Hasan, "Beyond the Barriers of Light Penetration: Strategies, Perspectives and Possibilities for Photodynamic Therapy," *Theranostics*, vol. 6, no. 13, pp. 2458–2487, 2016.